

The Present and Future of the West African Monsoon: A Process-Oriented Assessment of CMIP5 Simulations along the AMMA Transect

ROMAIN ROEHRIG, DOMINIQUE BOUNIOL, AND FRANCOISE GUICHARD

CNRM-GAME, Toulouse, France

FRÉDÉRIC HOURDIN

LMD, IPSL, Paris, France

JEAN-LUC REDELSPERGER

LPO, Brest, France

(Manuscript received 27 July 2012, in final form 22 February 2013)

ABSTRACT

The present assessment of the West African monsoon in the models of the Coupled Model Intercomparison Project (CMIP) phase 5 (CMIP5) indicates little evolution since the third phase of CMIP (CMIP3) in terms of both biases in present-day climate and climate projections.

The outlook for precipitation in twenty-first-century coupled simulations exhibits opposite responses between the westernmost and eastern Sahel. The spread in the trend amplitude, however, remains large in both regions. Besides, although all models predict a spring and summer warming of the Sahel that is 10%–50% larger than the global warming, their temperature response ranges from 0 to 7 K.

CMIP5 coupled models underestimate the monsoon decadal variability, but SST-imposed simulations succeed in capturing the recent partial recovery of monsoon rainfall. Coupled models still display major SST biases in the equatorial Atlantic, inducing a systematic southward shift of the monsoon. Because of these strong biases, the monsoon is further evaluated in SST-imposed simulations along the 10°W–10°E African Monsoon Multidisciplinary Analysis (AMMA) transect, across a range of time scales ranging from seasonal to intraseasonal and diurnal fluctuations.

The comprehensive set of observational data now available allows an in-depth evaluation of the monsoon across those scales, especially through the use of high-frequency outputs provided by some CMIP5 models at selected sites along the AMMA transect. Most models capture many features of the African monsoon with varying degrees of accuracy. In particular, the simulation of the top-of-atmosphere and surface energy balances, in relation with the cloud cover, and the intermittence and diurnal cycle of precipitation demand further work to achieve a reasonable realism.

1. Introduction

During the second half of the twentieth century, Africa witnessed one of the largest interdecadal climate signals of the recent observational records. The severe drying of the Sahel, which culminated in the devastating drought of 1984, plagued the region from the 1970s to the 1980s (e.g., Nicholson 1980; Nicholson et al. 2000; Held et al. 2005). In the recent decade, the Sahel transitioned to a period

with somewhat more abundant rainfall, suggesting a possible shift to a more favorable climate regime over the coming decades (Paeth and Hense 2004). However, at the same time, global mean temperature is increasing in response to increasing atmospheric greenhouse gases, so that predicting the evolution of Sahel rainfall from a range of a few decades to the end of the twenty-first century becomes urgently needed for developing adaptation strategies.

Such climate projections, as well as our physical understanding of the Sahel rainfall variability, mostly rely on general circulation models, characterized by a wide variety of complexity, from atmosphere-only models to the most recent Earth system models (ESMs). The regional response to global warming was uncertain in the

Corresponding author address: Romain Roehrig, Météo-France, CNRM-GAME/GMGEC/EAC, 42 avenue G. Coriolis, 31057 Toulouse CEDEX, France.
E-mail: romain.roehrig@meteo.fr

models of the third phase of the Coupled Model Intercomparison Project (CMIP3; Meehl et al. 2007b) used for the Fourth Assessment Report (AR4) of the Intergovernmental Panel on Climate Change (IPCC), which even disagree on the sign of future rainfall anomalies over the Sahel (e.g., Biasutti and Giannini 2006; Lau et al. 2006). This disagreement remains even among models that reasonably simulate the twentieth-century West African climate (Cook and Vizy 2006).

In fact, many of the previous generation of climate models failed in capturing major features of the West African climatology and variability, damping our confidence in their climate projection. One of the reasons is likely linked to the high spatial and temporal heterogeneities of the rainfall distribution across West Africa. In the Sahel, which lies at the northernmost extent of the West African monsoon (WAM), between 10° and 20°N, precipitation is highly sensitive to the intertropical convergence zone (ITCZ) latitudinal mean position during summer. There, rainfall is mainly supplied by mesoscale convective systems, often organized within synoptic disturbances such as African easterly waves (e.g., Kiladis et al. 2006).

Several studies emphasized the inability of current coupled or atmospheric models to correctly handle the main WAM characteristics. Cook and Vizy (2006) show that one-third of CMIP3 models do not simulate a WAM system (i.e., they do not capture properly the summer northward migration of the ITCZ over the continent). Atmospheric regional and global models, forced by observed sea surface temperatures (SSTs), analyzed within the framework of the African Monsoon Multidisciplinary Analysis (AMMA) Model Intercomparison Project (AMMA-MIP; Hourdin et al. 2010), the West African Monsoon Modeling and Evaluation (WAMME; Xue et al. 2010) project, and the African component of the Coordinated Regional Climate Downscaling Experiment (CORDEX-Africa; Jones et al. 2011; Nikulin et al. 2012) are generally more skillful, even though large biases in rainfall and the meridional circulation remain (Hourdin et al. 2010; Xue et al. 2010; Boone et al. 2010).

In the framework of the fifth phase of the Coupled Model Intercomparison Project (CMIP5), a new ensemble of state-of-the-art climate models is now available (Taylor et al. 2012), and this raises several questions. Do they agree more on Sahel rainfall projections? Do they capture the partial rainfall recovery observed over the last decades? How well are they able to reproduce the main features of the WAM? In the following, the CMIP5 ensemble is used to address these questions, assess the results of the modeling community efforts, and emphasize the challenges that remain for simulating the WAM. Our analysis indicates that over West Africa, CMIP5 models have not reached yet a degree of maturity that makes it

possible to directly rely on them to anticipate climate changes and their impacts, especially with regard to rainfall.

The present study is also motivated by the recent progress in the observation and understanding of the WAM, thanks to the AMMA program (Redelsperger et al. 2006). The AMMA observational strategy (Lebel et al. 2010) documented a meridional transect extending from the Gulf of Guinea to the Sahara desert, along the Greenwich meridian. Three preexisting surface-observing supersites along this transect were reinforced: the Upper Ouémé Valley, Niamey, and Gourma AMMA-Couplage de l'Atmosphère Tropicale et du Cycle Hydrologique (CATCH) sites (e.g., Lebel et al. 2009). This transect was used within the AMMA-MIP framework to evaluate regional and global models (Hourdin et al. 2010).

As part of the Cloud Feedback Model Intercomparison Project (CFMIP) component of CMIP5, participating centers also provided output at very high frequency (30 min or model time step) on a series of 119 grid points around the world, in order to better understand the climate model behaviors and their dependence on model formulation (Bony et al. 2011). Among these sites, 11 were defined in coordination with the AMMA community along the AMMA transect, 3 of them corresponding to the supersites mentioned above. In addition, the availability of new spaceborne measurements from active sensors as part of the afternoon satellite constellation (A-Train) opens the path for the establishment of global climatologies of the three-dimensional distribution of clouds (e.g., Bouniol et al. 2012). The availability of these new datasets and new outputs at selected sites from CMIP5, as well as the better understanding of some key processes at work in the WAM system, provides a unique opportunity to evaluate more in depth the WAM representation by climate models. In the present work, we seek to capitalize on this AMMA legacy, and to provide a process-oriented analysis of CMIP5 simulations.

The paper is organized as follows: Section 2 describes the datasets used for the CMIP5 model evaluation. In section 3, the long-term variability of the WAM is assessed from CMIP3 to CMIP5 models. Section 4 evaluates the representation of the WAM mean state and seasonal evolution in both coupled and SST-forced simulations. Section 5 addresses a more physical evaluation of monsoon processes, with an emphasis on the intraseasonal and diurnal scales of the water cycle. Finally, conclusions are given in section 6.

2. Datasets

a. Climate models from CMIP3 and CMIP5

In the present work, we consider a wide range of output from climate models that participated in CMIP3 and CMIP5. Climate change scenarios of CMIP3 [Special

Report on Emissions Scenarios (SRES) A2] and of CMIP5 [representative concentration pathways (RCPs) 4.5 and 8.5], in comparison with historical simulations [the twentieth-century simulation (20C3M) for CMIP3, “Historical” (Hist) for CMIP5] are used to assess the West African monsoon response to an increase of the CO₂ atmospheric concentration. SST-imposed or Atmospheric Model Intercomparison Project (AMIP)-type simulations are used to further analyze the representation of the WAM in the state-of-the-art models of the CMIP5 archive. Pre-industrial control runs (PiControl) with constant forcing are used for some CMIP5 models, to infer the decadal and interannual variability of Sahel precipitation.

A full description of the CMIP3 framework and a comprehensive assessment of the models can be found in Meehl et al. (2007b). Integrations of 18 CMIP3 models are used here. They were made available to the community by the Program for Climate Model Diagnosis and Intercomparison (PCMDI) through their website ([www-pcmdi.llnl.gov/ipcc/model_documentation/ipcc_model_documentation.php](http://pcmdi.llnl.gov/ipcc/model_documentation/ipcc_model_documentation.php)), where a detailed description of the models can be found. (All model names referred to in this paper are expanded in full in the appendix.)

The simulations performed as part of CMIP5 and used in the present study are listed in Table 1. They were made available on the Earth System Grid (ESG; <http://cmip-pcmdi.llnl.gov/cmip5/index.html>) data archive. The different types of integrations of the CMIP5 framework are described in Taylor et al. (2012). As we provide hereafter a more detailed evaluation of the CMIP5 AMIP simulations, Table 2 reports grid information of the atmospheric component of the models that provided this experiment.

b. Observational datasets

The present paper assesses several time scales in CMIP5 models, from the multidecadal variability to the diurnal cycle. Therefore a wide number of datasets for each targeted variable is used to account for these scales and for the uncertainty of observations. Their main characteristics are described in Table 3.

3. Long-term variability of the WAM from CMIP3 to CMIP5

a. Climate projection of temperature and precipitation over the Sahel

The CMIP3 exercise confirmed the high probability of a significant global warming at global scale as a consequence of anthropic greenhouse gas emissions (e.g., Meehl et al. 2007a). Some robust features in the spatial distribution of the associated climate changes were also

highlighted: a stronger warming over continents than over oceans, a stronger warming in high latitudes than in the tropics, and, in general, a tendency to reinforcement of rainfall contrasts in the tropics, with the ITCZ becoming more rainy and the subtropical subsiding anticyclonic belts becoming drier (e.g., Chou et al. 2009). However, a major issue was raised as models did not achieve any consensus for regional rainfall changes, in particular over the Sahel (Cook 2008).

Hereafter, we give a brief outlook of the changes over the Sahel as simulated by the new CMIP5 ensemble (Fig. 1). Similarly to the CMIP3 ensemble mean under the SRES A2 scenario (Fig. 1a), the CMIP5 ensemble mean (Fig. 1d) predicts under the RCP8.5 scenario a warming with a marked meridional gradient, the warming being higher over the Sahara than near the Guinean coast. This gradient is positioned over the Sahel, between 10° and 18°N, and corresponds to a large intermodel standard deviation, indicating a large uncertainty in the Sahel temperature increase. Associated with this warming, a drying is predicted by the ensemble mean over the Sahel west of 5°W whereas a wetting is predicted east of 5°W. The precipitation response remain qualitatively the same between CMIP3 and CMIP5, with a slight positive offset at the regional scale in the CMIP5 RCP8.5 scenario compared to the CMIP3 SRES A2 scenario. Note that these two scenarios are distinct, so that the response amplitude in temperature and precipitation cannot be quantitatively compared. The intermodel standard deviation of the precipitation mean changes among the models is generally as large as the precipitation changes themselves.

The consensus on the westernmost Sahel (15°–5°W) drying is relatively high, with about 80% of CMIP5 models agreeing on the sign of the change (Fig. 1f). It was similar in the CMIP3 ensemble (Fig. 1c). The drying remains moderate for most of the models being lower than 20% (Fig. 2a). In contrast, the consensus on the wetting over the eastern West Sahel (0°–10°E) has been slightly reduced from CMIP3 to CMIP5 (Figs. 1c,e and 2b), while it has clearly increased over the central/eastern Sahel (10°–35°E), with now more than 75% of the CMIP5 models agreeing on the positive sign of precipitation changes (Figs. 1c,e and 2c). The apparent low sign agreement in the transition region between the westernmost Sahel and the eastern West Sahel is likely related to the weak projected precipitation changes there. Note that the choice of the three averaging domains (Fig. 2) was conveyed by the sign agreement of the precipitation changes (Fig. 1) and some previous works that defined homogeneous regions over the Sahel at interannual to multidecadal time scales (e.g., Ward 1998; Lebel and Ali 2009). For some models, it might not be the most appropriate, in particular for those that do not

TABLE 1. CMIP5 simulations used in the present study. See appendix for complete expansions of model names.

Centers	Models	Simulations
Beijing Climate Center (BCC; China)	BCC-CSM1.1 BCC-CSM1.1(m)	AMIP,* Hist, RCP4.5, RCP8.5, PiControl Hist, RCP4.5, RCP8.5
Canadian Centre for Climate Modelling and Analysis (CCCma; Canada)	CanAM4 CanCM4 CanESM2	AMIP*** Hist Hist, RCP4.5
Centro Euro-Mediterraneo per I Cambiamenti Climatici (CMCC; Italy)	CMCC-CM CMCC-CESM CMCC-CMS	AMIP,* Hist, RCP4.5, RCP8.5, PiControl Hist, RCP4.5, RCP8.5 Hist, RCP8.5
Centre National de Recherches Météorologiques (CNRM)–Centre Européen de Recherche et de Formation Avancée en Calcul Scientifique (CERFACS; France)	CNRM–CM5	AMIP,* Hist, RCP4.5, RCP8.5, PiControl
Commonwealth Scientific and Industrial Research Organisation (CSIRO)–Bureau of Meteorology (BOM; Australia)	ACCESS1.0 ACCESS1.3	AMIP, Hist, RCP4.5, RCP8.5, PiControl AMIP, Hist, RCP4.5, RCP8.5, PiControl
CSIRO–Queensland Climate Change Centre of Excellence (QCCE; Australia)	CSIRO–Mk3.6.0	AMIP,* Hist, RCP4.5, RCP8.5, PiControl
First Institute of Oceanography (FIO; China)	FIO-ESM	Hist, RCP4.5, RCP8.5
Global Change and Earth System Science (GCESS; China)	BNU-ESM	AMIP,* Hist, RCP8.5, PiControl
European Consortium (EC)	EC-EARTH	AMIP,* Hist, PiControl
Institute of Numerical Mathematics (INM; Russia)	INM-CM4	AMIP,* Hist, RCP4.5, RCP8.5, PiControl
L’Institut Pierre-Simon Laplace (IPSL; France)	IPSL-CM5A-LR IPSL-CM5A-MR IPSL-CM5B-LR	AMIP,* Hist, RCP4.5, RCP8.5, PiControl AMIP,* Hist, RCP4.5, RCP8.5, PiControl AMIP,* Hist, RCP4.5, RCP8.5, PiControl
State Key Laboratory of Numerical Modeling for Atmospheric Sciences and Geophysical Fluid Dynamics (LASG)–Center for Earth System Science (CESS; China)	FGOALS-g2	AMIP,* Hist, RCP4.5, RCP8.5, PiControl
LASG–Institute of Atmospheric Physics (IAP; China)	FGOALS-s2	AMIP,* Hist, RCP4.5, RCP8.5, PiControl
Model for Interdisciplinary Research on Climate (MIROC; Japan)	MIROC4h MIROC5 MIROC-ESM MIROC-ESM-CHEM	Hist AMIP,* Hist, RCP4.5, RCP8.5, PiControl Hist, RCP4.5, RCP8.5 Hist, RCP4.5, RCP8.5
Met Office Hadley Centre (MOHC; United Kingdom)	HadCM3 HadGEM2-A HadGEM2-CC HadGEM2-ES	Hist AMIP*** Hist, RCP4.5, RCP8.5 Hist, RCP4.5, RCP8.5
Max Planck Institute for Meteorology (MPI-M; Germany)	MPI-ESM-LR MPI-ESM-MR MPI-ESM-P	AMIP,* Hist, RCP4.5, RCP8.5, PiControl AMIP,* Hist, RCP4.5, RCP8.5, PiControl Hist
Meteorological Research Institute (MRI; Japan)	MRI-AGCM3.2H MRI-AGCM3.2S MRI-CGCM3	AMIP* AMIP* AMIP,* Hist, RCP4.5, RCP8.5, PiControl
National Aeronautics and Space Administration (NASA)–Goddard Institute for Space Studies (GISS; United States)	GISS-E2-H GISS-E2-R GISS-E2-H-CC GISS-E2-R-CC	Hist, RCP4.5, RCP8.5 AMIP, Hist, RCP4.5, RCP8.5, PiControl Hist, RCP4.5 Hist, RCP4.5
National Center for Atmospheric Research (NCAR; United States)	CCSM4	AMIP, Hist, RCP8.5, PiControl
Norwegian Climate Centre (NCC; Norway)	NorESM1-M NorESM1-ME	AMIP,* Hist, RCP4.5, RCP8.5, PiControl Hist, RCP4.5, RCP8.5
National Institute of Meteorological Research (NIMR)–Korea Meteorological Administration (KMA; South Korea)	HadGEM2-AO	Hist, RCP4.5, RCP8.5

TABLE 1. (Continued)

Centers	Models	Simulations
National Oceanic and Atmospheric Administration (NOAA)/Geophysical Fluid Dynamics Laboratory (GFDL; United States)	GFDL-CM2p1	Hist
	GFDL-CM3	Hist, RCP4.5, RCP8.5
	GFDL-ESM2G	Hist, RCP4.5, RCP8.5
	GFDL-ESM2M	Hist, RCP4.5, RCP8.5
	GFDL-HIRAM-C180	AMIP*
	GFDL-HIRAM-C360	AMIP*
National Science Foundation (NSF)–Department of Energy (DOE)–National Center for Atmospheric Research (NCAR; United States)	CESM1(BGC)	Hist, RCP4.5, RCP8.5
	CESM1(CAM5)	AMIP, Hist, RCP4.5, RCP8.5, PiControl
	CESM1(FASTCHEM)	Hist
	CESM1(WACCM)	Hist

* Daily outputs are available for these simulations.

** High-frequency output is used at selected sites.

capture the right position of the summer ITCZ (see section 4). A more detailed analysis of the projections is required but remains out of the scope of the present study.

East of 0°, the CMIP5 ensemble mean precipitation response is partly dominated by about four or five models that simulates a strong increase of precipitation, greater than 60%. Those models also predict a relatively weak warming over the Sahel, and even some cooling for one of them over the eastern Sahel. In the RCP8.5 scenario, their July–September (JAS) values of ΔT_{2m} and $\Delta P/P$ (P being

precipitation) over the central–eastern Sahel are 2.9 K and 62% for MIROC5, 0.2 K and 86% for BNU-ESM, 0.2 K and 103% for FGOALS-g2, -1.0 K and 103% for MIROC-ESM, and 2.7 K and 109% for MIROC-ESM-CHEM; while the values of all other models range over 4.5 ± 1.5 K and $0\% \pm 30\%$. Most projections thus indicate moderate changes in the pessimistic scenario, to be compared with the 40% decrease observed between the 1950s–60s and 1970s–80s, and the +20% rainfall recovery in recent years over parts of the Sahel (Lebel and Ali 2009).

TABLE 2. Characteristics of AMIP simulation models used in the present study.

Models	Reference	Horizontal grid	Number of vertical levels
ACCESS1.0; ACCESS1.3	http://wiki.csiro.au/confluence/display/ACCESS/	$1.875^\circ \times 1.25^\circ$	38
BCC-CSM1.1	Wu et al. (2010)	T42 ($2.8^\circ \times 2.8^\circ$)	26
BNU-ESM	http://esg.bnu.edu.cn/BNU_ESM_webs/htmls/index.html	T42 ($2.8^\circ \times 2.8^\circ$)	26
CanAM4	http://www.ec.gc.ca/cmacc-cccma/	T63 ($1.875^\circ \times 1.875^\circ$)	35
CCSM4	Neale et al. (2010a); Gent et al. (2011)	$0.9^\circ \times 1.25^\circ$	26
CESM1(CAM5)	Neale et al. (2010b)	$0.5^\circ \times 1.25^\circ$	30
CMCC-CM	http://www.cmcc.it/data-models/models	$0.75^\circ \times 0.75^\circ$	31
CNRM-CM5	Volodire et al. (2013)	T127 ($1.4^\circ \times 1.4^\circ$)	31
CSIRO-Mk3.6.0	Rotstayn et al. (2010)	T63 ($1.875^\circ \times 1.875^\circ$)	18
EC-EARTH	Hazeleger et al. (2010)	T159 ($1.125^\circ \times 1.125^\circ$)	62
FGOALS-g2	http://www.lasg.ac.cn/FGOALS/CMIP5	$2.8^\circ \times 2.8^\circ$	26
FGOALS-s2	http://www.lasg.ac.cn/FGOALS/CMIP5	$1.7^\circ \times 2.8^\circ$	26
GFDL-HIRAM-C180	Donner et al. (2011)	$0.5^\circ \times 0.5^\circ$	32
GFDL-HIRAM-C360	Donner et al. (2011)	$0.25^\circ \times 0.25^\circ$	32
GISS-E2-R	http://data.giss.nasa.gov/modelE/ar5	$2^\circ \times 2.5^\circ$	40
HadGEM2-A	Collins et al. (2008)	$1.25^\circ \times 1.875^\circ$	38
INM-CM4	Volodin et al. (2010)	$1.5^\circ \times 2.5^\circ$	21
IPSL-CM5A-LR	Dufresne et al. (2013)	$1.895^\circ \times 3.75^\circ$	39
IPSL-CM5A-MR	Dufresne et al. (2013)	$1.25^\circ \times 2.5^\circ$	39
IPSL-CM5B-LR	Hourdin et al. (2012)	$1.895^\circ \times 3.75^\circ$	39
MIROC5	Watanabe et al. (2010)	T85 ($1.4^\circ \times 1.4^\circ$)	40
MPI-ESM-LR	http://www.mpimet.mpg.de/en/science/models/mpi-esm.html	T63 ($1.875^\circ \times 1.875^\circ$)	47
MPI-ESM-MR	http://www.mpimet.mpg.de/en/science/models/mpi-esm.html	T63 ($1.875^\circ \times 1.875^\circ$)	95
MRI-AGCM3.2H	Mizuta et al. (2012)	T319 ($0.56^\circ \times 0.56^\circ$)	64
MRI-AGCM3.2S	Mizuta et al. (2012)	T959 ($0.19^\circ \times 0.19^\circ$)	64
MRI-CGCM3	Yokimoto et al. (2011)	T159 ($1.125^\circ \times 1.125^\circ$)	48
NorESM1-M	Kirkevåg et al. (2008)	$1.9^\circ \times 2.5^\circ$	26

TABLE 3. Observational datasets.

Variables	Dataset	References	Resolution	Frequency	Period covered
Rainfall	CRU version 3.1	Mitchell and Jones (2005)	$0.5^\circ \times 0.5^\circ$	Monthly	1901–2008
	CMAP	Xie and Arkin (1997)	$2.5^\circ \times 2.5^\circ$	Monthly	1979–2008
	GPCP	Huffman et al. (2001)	$1^\circ \times 1^\circ$	Daily	1997–2008
	TRMM-3B42	Huffman et al. (2007)	$0.25^\circ \times 0.25^\circ$	Daily	1998–2008
	Ouémé rain gauges (9.5°N, 2°E)	Le Lay and Galle (2005); Depraetere et al. (2009)	Site ^a	5 and 30 min	1999–2011
	Niamey rain gauges (13.5°N, 2.2°E)	Lebel et al. (2010)	Site ^a	5 and 30 min	1990–2011
Convection	NOAA OLR	Liebmann and Smith (1996)	$2.5^\circ \times 2.5^\circ$	Daily	1979–2008
Clouds	<i>CloudSat-CALIPSO</i>	Bouniol et al. (2012)	AMMA transect ^b	Monthly	2006–10
	ARM Mobile Facility (AMF)	Miller and Slingo (2007); Bouniol et al. (2012)	Niamey site	30 min	2006
Radiation	CERES EBAF ^c edition 2.6	Wielicki et al. (1996); Loeb et al. (2009)	$1^\circ \times 1^\circ$	Monthly	2000–10
	NASA-GEWEX SRB release 3.0 (pr and qc) ^d	Stackhouse et al. (2011)	$1^\circ \times 1^\circ$	Monthly	1983–2007
	Transect sites ^e	Lebel et al. (2009); http://www.amma.catch.org	Sites	JAS average	
2-m temperature	CRU version 3.1	Mitchell and Jones (2005)	$0.5^\circ \times 0.5^\circ$	Monthly	1979–2008
	NCEP CFSR	Saha et al. (2010)	$1^\circ \times 1^\circ$	Monthly/daily	1979–2008
	NASA-MERRA	Rienecker et al. (2011)	$1^\circ \times 1^\circ$	Monthly/daily	1979–2008
	ERA-Interim	Simmons et al. (2007)	$0.75^\circ \times 0.75^\circ$	Monthly/daily	1979–2008

^a The number and density of gauges vary from year to year. To match the 30-min model output resolutions extracted at these selected sites, and not oversample any particular region, the data were resampled and spatially homogenized in a $0.2^\circ \times 0.2^\circ$ domain within a $2^\circ \times 2^\circ$ area around both sites.

^b Each satellite track within a 10°W – 10°E domain is assumed representative of the Greenwich latitude, leading to at least two sampling per day along this transect.

^c The Clouds and Earth's Radiant Energy System (CERES) Energy Balanced and Filled (EBAF) edition 2.6 product consists of top-of-atmosphere and surface radiative fluxes (<http://ceres.larc.nasa.gov>).

^d The National Aeronautics and Space Administration (NASA)-Global Energy and Water Cycle Experiment (GEWEX) surface radiation budget (SRB) consists of top-of-atmosphere and surface radiative fluxes. Two sets of surface radiative flux estimations are available, based on different algorithms, known as primary (SRB3pr) and Langley parameterized algorithms (SRB3qc). More information on these two datasets is available at <http://gewex-srb.larc.nasa.gov/index.php>.

^e Bamba (17.1°N , 1.4°E , 2004–07), Agoufou (15.34°N , 1.48°E , 2002–08), Wankama (13.67°N , 2.65°E , 2005–06), Bira (9.82°N , 1.71°E , 2006), Naholou (9.73°N , 1.60°E , 2006), and a Prediction and Research Moored Array in the Tropical Atlantic (PIRATA) buoy (0° , 0° , 2006, only incoming shortwave at surface).

The temperature and precipitation changes are likely related. Reinforced rainfall should moderate the temperature increase in summer, through an increase of surface latent heat flux. Figures 2e and 2f are consistent with this interpretation. In the dry March–May (MAM) season, the Sahel warming reflects mostly an amplification of the global warming response by $30\% \pm 20\%$. In contrast, the projected summer Sahelian warming displays much more spread than the global warming, emphasizing a coupling with the rainfall response. Three models that predict a significant increase of Sahel rainfall also predict a much weaker JAS warming than the global value.

b. Decadal and interannual rainfall variability over the Sahel

The Sahelian rainfall exhibits a large variability at decadal and interannual time scales. To address these

scales, the time series of the Sahel precipitation P was decomposed into a decadal component \bar{P}^D and an interannual fluctuation δP , such that $P = \bar{P}^D + \delta P$. The quantity \bar{P}^D is defined as the 9-yr running mean of the raw series. Figure 3a illustrates the observed raw and filtered time series of precipitation averaged over (10° – 18°N , 0° – 10°E) for both the Climatic Research Unit (CRU) and Climate Prediction Center (CPC) Merged Analysis of Precipitation (CMAP) datasets (see Table 3). The Sahelian drought is clearly identified after 1973, with a partial recovery in the recent years. Although this recovery is not homogeneous over the entire Sahelian belt, Lebel and Ali (2009) show a clear signal over this central Sahel domain.

The skill of CMIP5 models to reproduce this recent recovery is addressed in AMIP simulations through the computation of precipitation mean difference between the periods 2000–08 (wetter) and 1979–87 (drier; Fig. 3b,

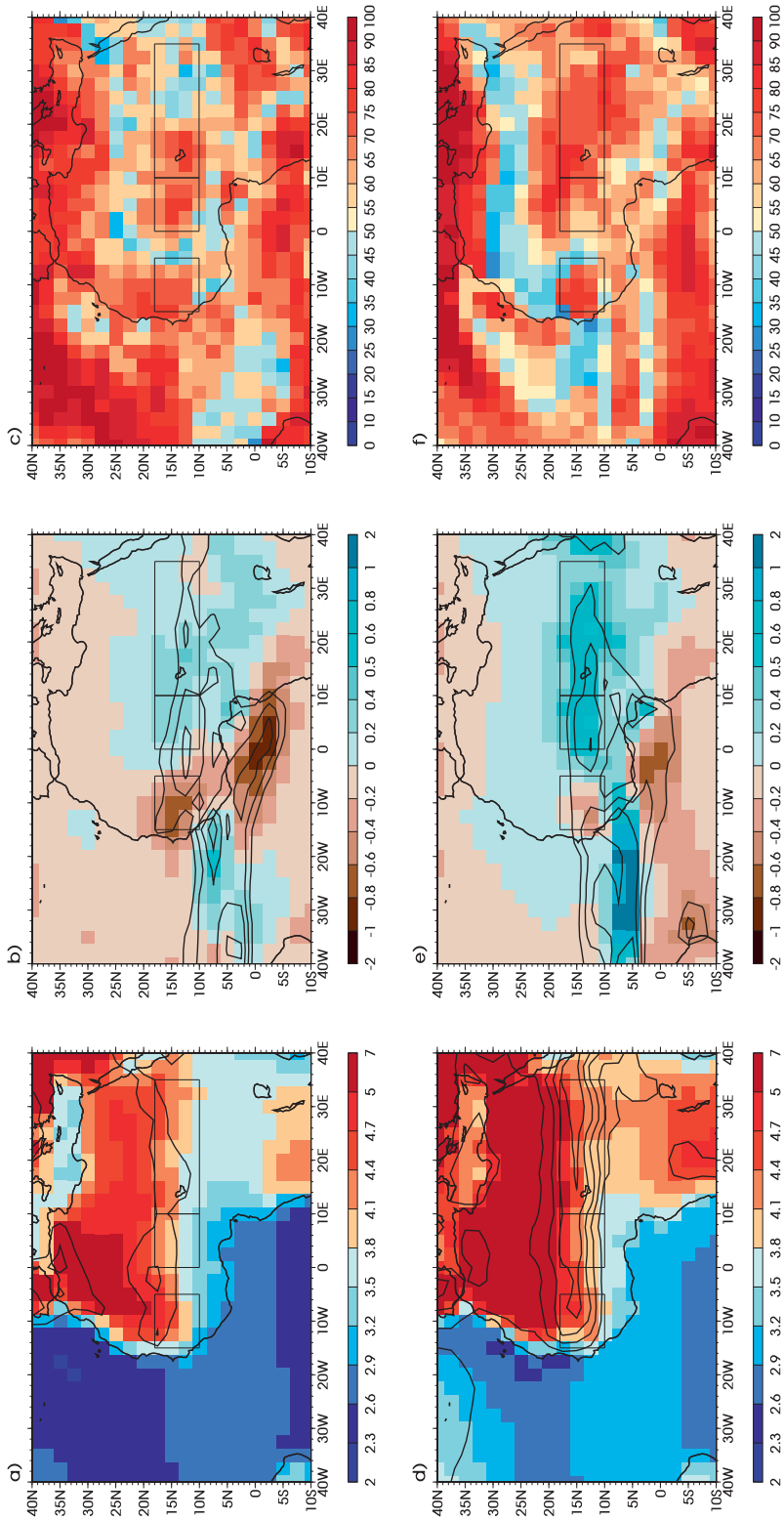


FIG. 1. (a) Climate projections of 2-m temperature (colors; K) plotted as the difference between the periods 2071–2100 and 1971–2000 for the CMIP3 SRES A2 ensemble mean. Contours show the CMIP3 intermodel standard deviation with one contour every 0.2 K, beginning at 1.0 K. (b) As in (a), but for precipitation (mm day⁻¹) and with one contour every 0.3 mm day⁻¹, beginning at 1.0 mm day⁻¹. (c) The percentage of the models in the CMIP3 ensemble that agree on the sign of the temperature changes. (d)–(f) As in (a)–(c), but for the CMIP5 RCP8.5 model ensemble.

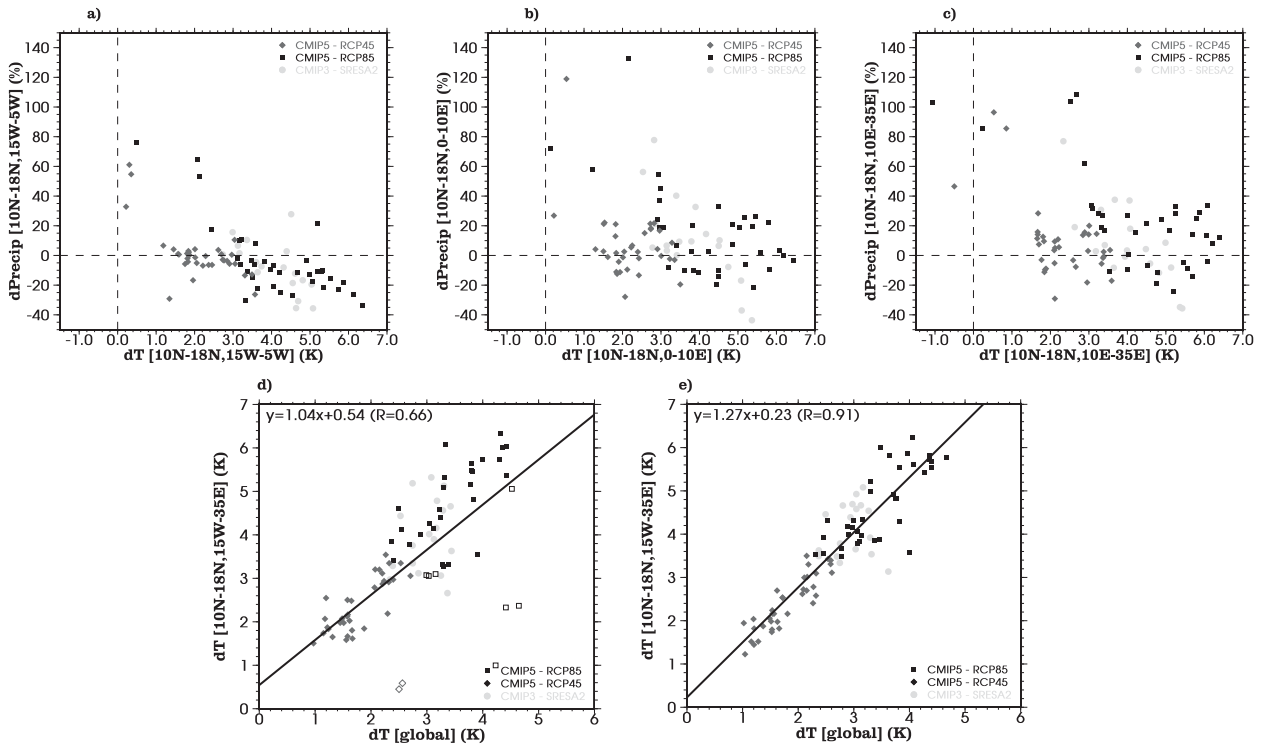


FIG. 2. (a) Climate precipitation projections (%) plotted against those of 2-m temperature (K) averaged over the westernmost Sahel grid box (10° – 18° N, 15° – 5° W) shown in Fig. 1a. The differences are computed between the periods 2071–2100 and 1971–2000 for the JAS season for the CMIP3 SRES A2 scenario, and the CMIP5 RCP4.5 and RCP8.5 scenarios. (b) As in (a), but for the central West Sahel grid box (10° – 18° N, 0° – 10° E). (c) As in (a), but for the central–eastern Sahel grid box (10° – 18° N, 10° – 35° E). (d) Climate projections of global 2-m temperature plotted against 2-m temperature averaged over the Sahel domain (10° – 18° N, 15° W– 35° E); white squares are projections of precipitation change $>25\%$. (e) As in (d), but for the MAM season.

dots). The relative change between these two periods ranges between 10% in the CRU dataset and 24% in the CMAP dataset. Despite a large dispersion, one-half of the models capture the tendency to rainfall recovery. Five have a tendency close to zero and three even simulate a significant negative tendency. This might be partly due to internal variability as illustrated with the five members of the IPSL-CM5A-LR AMIP ensemble (Fig. 3b), which predicts a recovery, ranging from +6% to +21%.

The reasonable skill of the AMIP simulations is probably related to the monsoon response to the change of SSTs, consistently with the success of several atmospheric models to reproduce the main outlines of the twentieth-century Sahel rainfall (e.g., Tippett and Giannini 2006; Hoerling et al. 2006).

The standard deviation of \bar{P}^0 in the PiControl and Historical experiments can be used to assess the skill of coupled atmosphere–ocean models to reproduce the observed decadal variability (Fig. 3b). In CRU observations, the standard deviation over the twentieth century reaches almost 10%. Most models underestimate

this amplitude, often by a factor of 2, in both types of experiments, with the notable exceptions of IPSL-CM5B-LR, which significantly overestimates the amplitude of the decadal variability, and of BCC-CSM1.1, which has an amplitude slightly higher than the observed one. It is also remarkable that the amplitude of decadal variability is highly consistent for each model across the two experiments, suggesting that decadal fluctuations in Historical runs are not forced by greenhouse gases, aerosols, or land use (for models including land-use changes).

Interannual variability of CMIP5 models is investigated based on the standard deviation of the interannual fluctuations δP (Fig. 3c). The observed value of 12% is consistent in CMAP and CRU observations. In the Historical and PiControl simulations, all models lie between 8%–17%, except ACCESS1.3 (22%), BCC-CSM1.1 (30%), CMCC-CM (22%), FGOALS-s2 (22%), IPSL-CM5B-LR (38%), and MRI-CGCM3 (20%), which overestimate interannual variability. The large amplitude of decadal variability in BCC-CSM1.1 and IPSL-CM5B-LR may be a consequence of this excessive year-to-year variability.

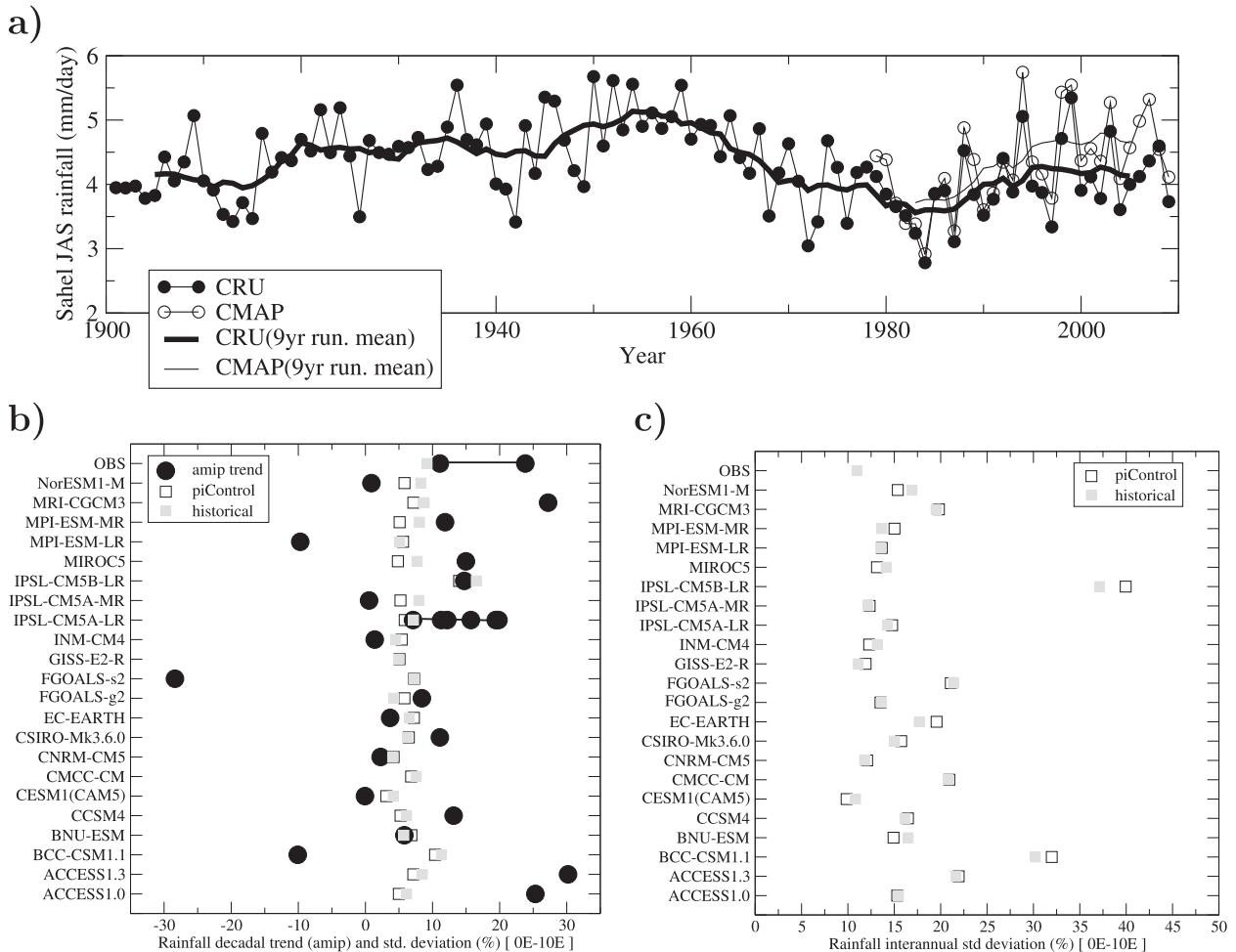


FIG. 3. (a) Time evolution of raw precipitation (mm day^{-1} , lines with dots) averaged over (10° – 18°N , 0° – 10°E) using CRU data (black dots) and CMAP (open dots), and its decadal component \bar{P}^9 (thick solid line), computed as the 9-yr running mean of the raw index. (b) Precipitation difference (%) between the 9-yr periods 2000–08 and 1979–87 for AMIP simulations (black dots) and standard deviation of \bar{P}^9 in historical (gray squares) and preindustrial control (open squares) experiments. The standard deviations (%) are computed on the full period (1850–2008) for historical simulations and on the available length for preindustrial simulations, which ranges from 250–1000 yr depending on the model. The standard deviation has been normalized by the mean \bar{P}^9 . For observations, the squares correspond to the normalized standard deviation of CRU \bar{P}^9 while the two black circles correspond to the precipitation difference (%) between the periods 2000–08 and 1979–87 in the CRU and CMAP observations. (c) Standard deviation of interannual fluctuation $\delta P = P - \bar{P}^9$ as a fraction of the mean precipitation (%), in preindustrial control (open squares) and historical (gray squares) experiments.

4. The representation of the West African monsoon mean state from CMIP3 to CMIP5

Most of the following analysis is based on the 10°W – 10°E AMMA transect, promoted by the AMMA observing strategy (Lebel et al. 2010) and the AMMA-MIP framework (Hourdin et al. 2010). Because of the small zonal variations in surface field meridional structure between 10°W and 10°E , this transect approach is well suited to analyze the WAM climatological structure. As a consequence, the term “Sahel” will be used hereafter in a *limited meaning* for the 10° – 18°N , 10°W – 10°E region. As

shown above, such a framework is not as appropriate to study the WAM interannual-to-long-term variability.

a. Precipitation bias in historical simulations and its relationship with surface air temperature

The sensitivity of the Sahelian rainfall to SSTs has important consequences on the skill of climate models to simulate properly the present-day mean state of the monsoon system. All coupled models suffer from significant and robust SST biases with respect to their AMIP version (Fig. 4). Most of them systematically display

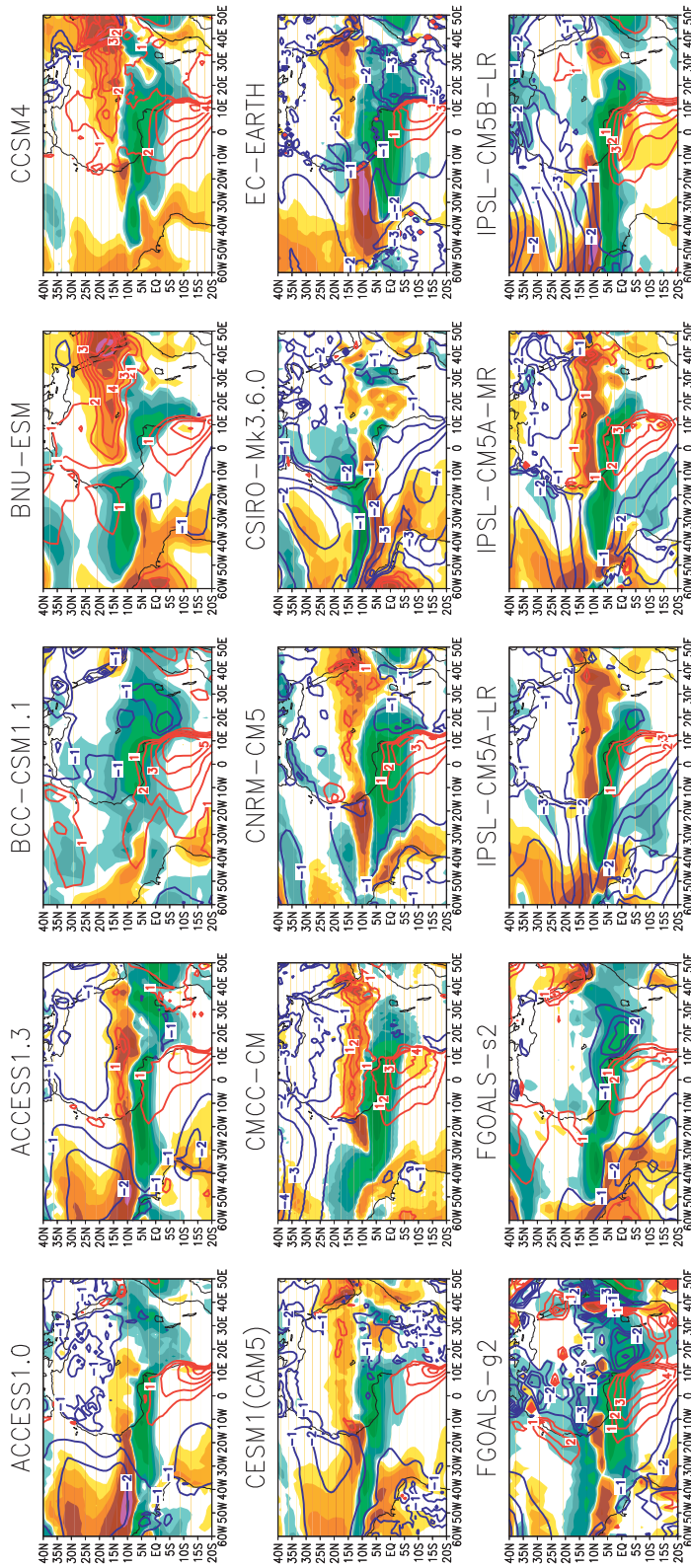


FIG. 4. Difference between historical and AMIP simulations for precipitation (shaded, mm day⁻¹) and 2-m temperature (contours every 1 K with the 0 contour omitted) averaged over the JAS seasons of the 1979–2008 period. The CMIP3 and CMIP5 ensemble means are shown in the bottom row, as well as the CMIP5 ensemble mean biases of historical and AMIP simulations against the GPCP dataset for precipitation and the ERA-Interim dataset for the 2-m temperature.

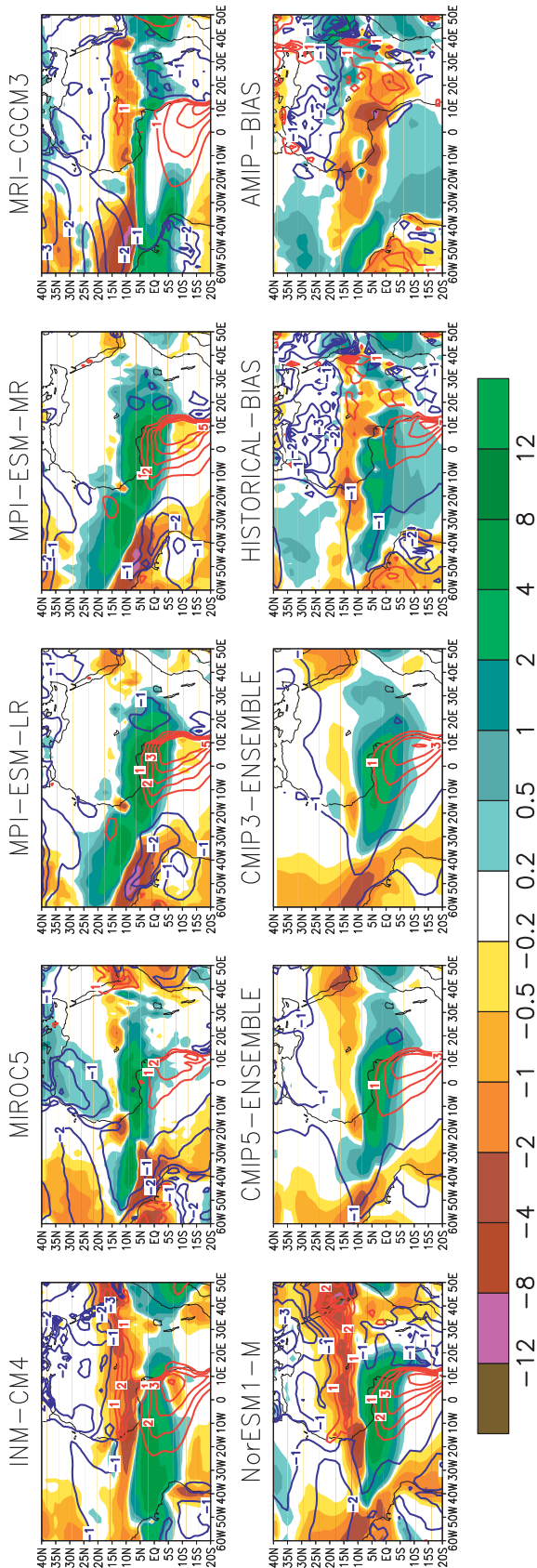


FIG. 4. (Continued)

strong warm biases (of several kelvin) over upwelling regions, on the eastern side of tropical oceanic basins, especially in the South Atlantic. The only exception is CSIRO-Mk3.6.0, which has a global cold bias over the ocean.

The CMIP5 ensemble mean warm bias (CMIP5-ENSEMBLE in Fig. 4) peaks at more than +3 K in the equatorial eastern Atlantic, contrasting with a cold bias of about -1 K in the North Atlantic. This systematic bias structure is remarkably similar to the CMIP3 ensemble mean (CMIP3-ENSEMBLE in Fig. 4).

This warm bias in the equatorial Atlantic has been shown to be partly responsible for the systematic southward shift of the ITCZ in coupled models (Richter and Xie 2008). It is associated with a strong reinforcement of rainfall over the Guinean coast and often a reduction over the Sahel, as illustrated in Fig. 4. Consistently, CSIRO-Mk3.6.0 shows an opposite signal, with slightly less rainfall over the Guinean coast.

The latitudinal position of the ITCZ over West Africa is, to some extent, related to the intensity of the north-south temperature gradient, which is partly driven by the SSTs in the equatorial Atlantic (Fig. 5). The correlation coefficient reaches 0.4 in historical CMIP5 simulations. AMIP simulations exhibit a similar relationship, with a smaller spread in the ITCZ position. The temperature over the Sahara is thus expected to play an important role too in the summer monsoon position. It will be further evaluated in section 4b(2).

To summarize, both CMIP3 and CMIP5 coupled models exhibit large biases in the mean position of the West African monsoon, which is likely associated with the warm SST bias in the equatorial Atlantic. This first-order, robust, and quasi-systematic bias prevents any further insight into the representation of key features and processes of the monsoon in coupled simulations. Therefore, we now focus on AMIP simulations, which display a weaker dispersion in the ITCZ summer position over West Africa (Fig. 5).

b. The WAM mean state in AMIP simulations

1) PRECIPITATION

Figure 6 shows JAS precipitation averaged from 1979 to 2008 between 10° W and 10° E for each model and observational dataset introduced in section 2. Even though the Global Precipitation Climatology Project (GPCP) and Tropical Rainfall Measuring Mission (TRMM) datasets do not cover the same period, they provide similar results along this transect, the sensitivity to the exact chosen period being much smaller than the typical model biases (not shown). Following the previous section and Fig. 5, models have been separated into

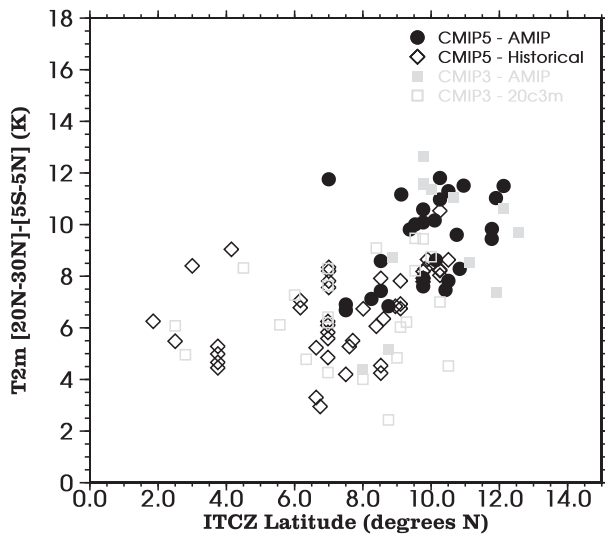


FIG. 5. Scatterplot of the ITCZ position versus the meridional temperature gradient between the Gulf of Guinea and the Sahara desert. The ITCZ latitude corresponds to the position during JAS of maximum precipitation averaged over 10°W – 10°E . The JAS temperature gradient is computed as the difference between (20° – 30°N , 10°W – 10°E) and (5°S – 5°N , 10°W – 10°E): CMIP5 AMIP (black circles), CMIP5 Historical (open diamonds), CMIP3 AMIP (gray squares), and CMIP3 20C3M (open squares).

two subsets according to their mean temperature over the Sahara: the warm (Fig. 6a) and the cold (Fig. 6b) models. Overall, models capture the large-scale precipitation maximum over the continent near 10° – 11°N . About one-third of the models (BCC-CSM1.1, FGOALS-s2, GISS-E2-R, HadGEM2-A, INM-CM4, the three IPSL-CM5 models, and MRI-CGCM3) locate their ITCZ a bit too much to the south, near 7° – 8°N . In contrast, only a few models reproduce the maximum amount of precipitation along the transect (8 mm day^{-1}). Five models overestimate this maximum by 1.5 – 4 mm day^{-1} (CSIRO-Mk3.6.0, GFDL-HIRAM-C180, GFDL-HIRAM-C360, IPSL-CM5A-MR, and MIROC5). Seven models underestimate it by 1 – 5 mm day^{-1} . Thus, only half of CMIP5 models are in qualitative agreement with observations. About one-half of the models underestimate the rainfall over the Sahel (i.e., north of 12°N), and most of these “too dry” models are also among the colder ones.

The high-resolution runs of GFDL-HIRAM (see Table 2) capture the monsoon latitudinal structure but exhibit similar skills to other models in reproducing the amplitude of precipitation. Besides, little sensitivity to the passage from a 0.5° (GFDL-HIRAM-C180) to a 0.25° (GFDL-HIRAM-C360) resolution is noticed. Enhanced vertical resolution from MPI-ESM-LR (47) to MPI-ESM-MR (95) results in a very similar ITCZ. In contrast, the modification of the physical packages from

IPSL-CM5A-LR to IPSL-CM5B-LR indicates a clear dependence on the formulation of the model physics, especially north of 10°N , where rainfall is decreased by almost a factor of 2 in IPSL-CM5B-LR.

2) TEMPERATURE AT 2 M AND THE SAHARAN HEAT LOW

The spread described in the previous section can be partly related to the meridional large-scale temperature gradient (section 4a; Fig. 5). In AMIP simulations, this gradient is driven at first order by the temperature in the Saharan heat low region, which is a key feature of the West African monsoon at the seasonal (Lavaysse et al. 2009) and intraseasonal (Chauvin et al. 2010) time scales. During the summer, a heat low establishes a low pressure system over the Sahara desert and acts to reinforce the moist monsoon flow over the Sahel. The Saharan heat low is also key in the maintenance of the African easterly jet in the midtroposphere (Thorncroft and Blackburn 1999). The associated temperature gradient is a source of baroclinic energy for African easterly waves, which affects rainfall at various time scales (e.g., Fink and Reiner 2003; Kiladis et al. 2006; Thorncroft and Rowell 1998). In particular, Ruti and Dell’Aquila (2010) showed that models characterized by a weak meridional temperature gradient are unable to feed these synoptic disturbances. A strong gradient, however, is not a necessary condition for arising waves.

Over the Sahara, the near-surface temperature in CMIP5 models exhibits a large spread, which reaches almost 7 K near 25°N (Fig. 7). This spread starts to develop in the southern Sahel, around 10°N , and extends up to the northern coast of Africa at 35°N . Unfortunately the dispersion is as large as in observational datasets and reanalyses. This reflects the sparse coverage of in situ observations over the Sahara, and precludes detailed model evaluation there. The surface energy budget over the Sahara discussed at the end of this section provides further insight into the origin of this spread within the CMIP5 ensemble. Up to 15°N , observations and reanalyses are in better agreement and the spread among models is weaker, although about one-third of CMIP5 models are still too cold by 2 – 3 K [BNU-ESM, CCSM4, CESM1(CAM5), CNRM-CM5, EC-EARTH, GFDL-HIRAM-C180 and -C360, MRI-AGCM3.2S, and NorESM1-M], and one is too warm by 2 – 3 K (MRI-CGCM3).

3) CLOUDS AND THEIR RADIATIVE EFFECT

Bouniol et al. (2012) analyzed the cloud cover mean properties over the Sahel with the AMF data of Niamey. They identified four cloud categories: clouds associated with convective systems and low-, mid-, and high-level clouds, in agreement with Slingo (1980). Using *CloudSat*

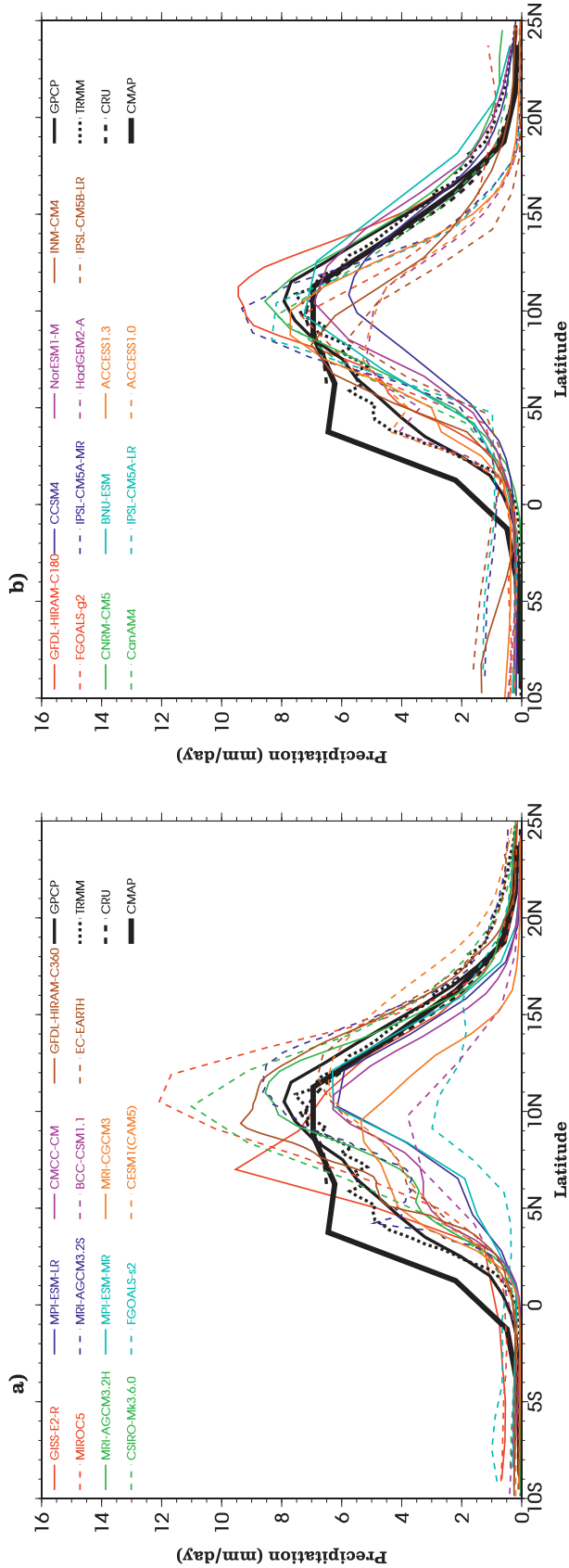


FIG. 6. Precipitation (mm day^{-1}) averaged over 10°W – 10°E for the JAS season for the years 1979–2008 for CMIP5 simulations, and 1997–2008 for GPCP, 1998–2008 for TRMM, 1979–2008 for CRU, and 1979–2008 for CMAP datasets. Each dataset is displayed using its own horizontal resolution. The left (right) panel corresponds to the warmer (colder) models over the Sahara (20° – 30°N , 10°W – 10°E).

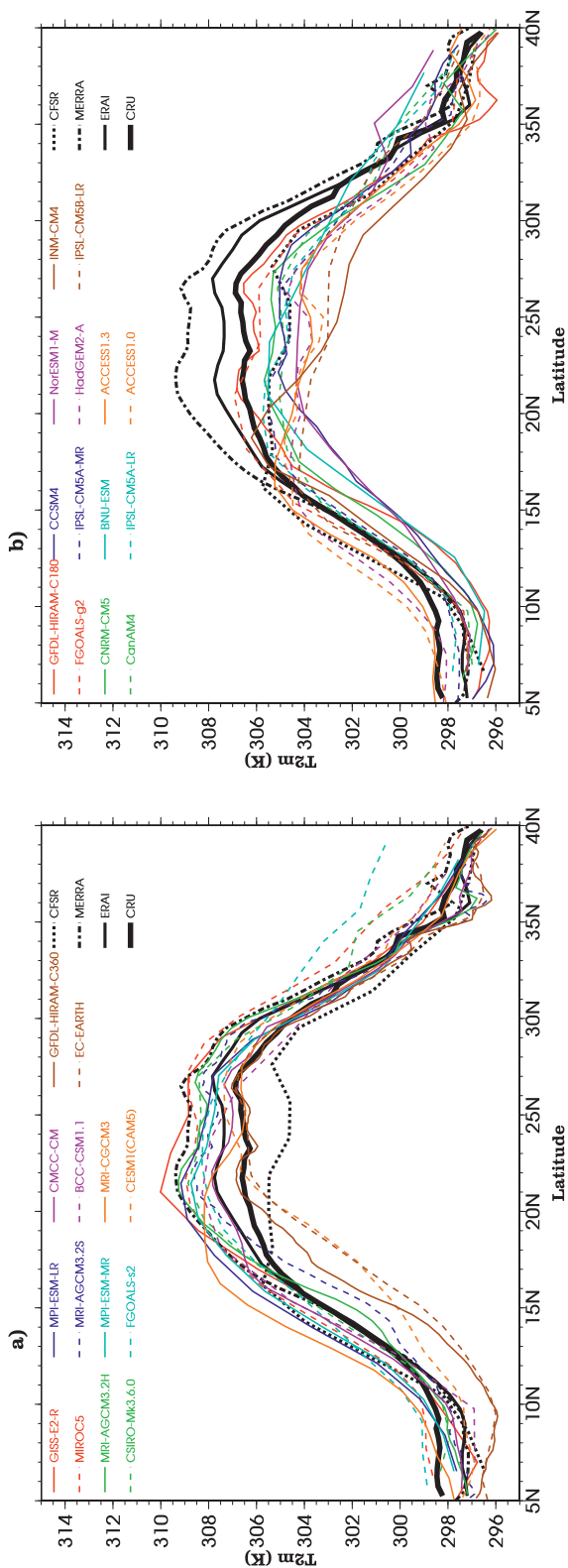


FIG. 7. As in Fig. 6, but for the 2-m temperature (K) for CMIP5 simulations, reanalyses, and CRU.

and *Cloud–Aerosol Lidar and Infrared Pathfinder Satellite Observations (CALIPSO)*, they also documented their seasonal cycle at the regional scale over West Africa, characterized by a northward migration of deep convective clouds associated with the ITCZ, low-level shallow clouds over the Sahel in summer, and the ubiquitous presence of midlevel and cirrus clouds. In addition, a 2-km-deep layer of stratocumulus is observed over the Gulf of Guinea. Figure 8 (top-left panel) presents the JAS climatological latitude–altitude cross section of the mean cloud fraction, built from five years of *CloudSat–CALIPSO* data. Note that the precipitating water phase was discarded in the observations.

All the models capture to some extent the observed cloud structure (Fig. 8). The maximum in cloud fraction related to the deep convective systems is collocated with the mean ITCZ position (Fig. 6), although some models do not reproduce the observed vertical extent of cloud fraction. Most models include in their cloud fraction only nonprecipitating condensed water, whereas in the observational dataset, the computed cloud fraction also accounts for precipitating particles, especially above the freezing level. Even dense aggregates found in convective anvils need about 50 min to fall down from the 8-km altitude to the freezing level at a 1 m s^{-1} fall speed (Bouniol et al. 2010). The apparent underestimation of cloud fraction in the midtroposphere in ACCESS1.3 or IPSL-CM5A-LR may thus partly originate from the lack of consideration given to precipitating ice as making part of the cloud (Waliser et al. 2011).

The high amount of midlevel clouds between 15° and 30°N is a specificity of the region. However, none of the models manages to reproduce the observed amount, even if some of them (CanAM4, IPSL-CM5B-LR, MIROC5) partly capture their occurrence. The stratocumuli over the Gulf of Guinea are also challenging most of the models. They are often not deep enough when they occur; and CNRM-CM5 and CanAM4 completely miss this cloud type.

The proper representation of these different cloud types is important for the regional energy budget and associated cloud feedbacks. Figure 9 shows the cloud radiative effect (CRE) at the top of the atmosphere. The longwave (LW) CRE is strongly shaped by the convective cloud cover amount and vertical structure, and the latitudinal shift of its maximum is clearly explained by the spread of the ITCZ JAS location (Fig. 6).

The shortwave (SW) CRE displays two minima associated with the stratocumulus clouds over the ocean and the ITCZ over the continent. The CRE spread across the simulations is larger in the shortwave than in the longwave. Most models overestimate this shortwave CRE over the ocean except CNRM-CM5, due to a lack

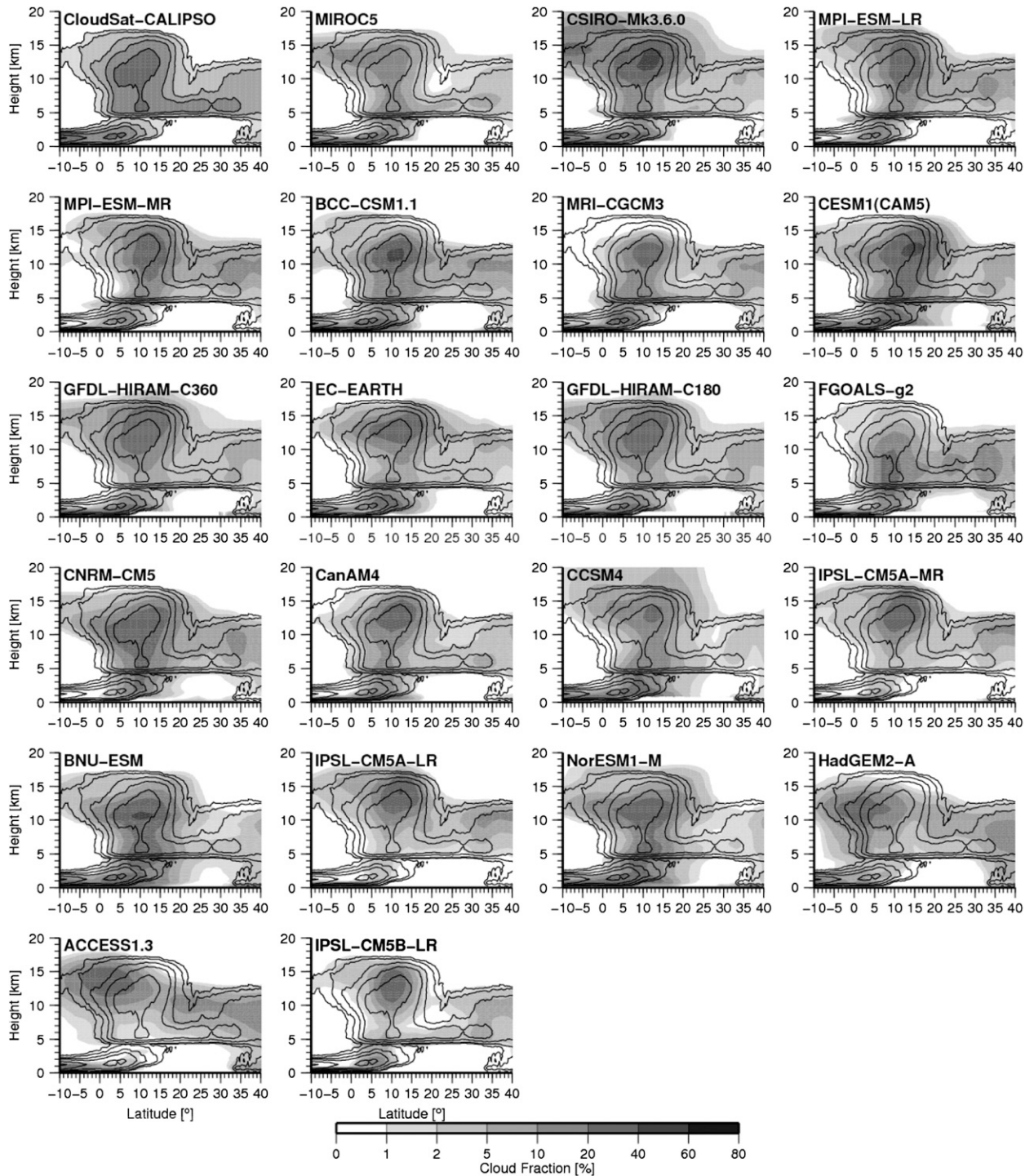


FIG. 8. Latitude–height plots of cloud fraction averaged between 10°W and 10°E for the JAS season for the years 2006–10 for the *CloudSat*–*CALIPSO* dataset and 1979–2008 for the models. Models are organized (top left)–(bottom right) from the warmest over the Sahara (20° – 30°N , 10°W – 10°E) to the coldest.

of stratocumulus clouds there (Fig. 8). Further north, within the ITCZ, the two IPSL models and HadGEM2-A underestimate the CRE, and IPSL-CM5A-LR shows little response to the cloud cover increase with latitude.

Even though shortwave and longwave CRE partly compensate each other, they have a distinct latitudinal structure. The longwave CRE maximum is shifted 5° northward compared to the shortwave CRE minimum.

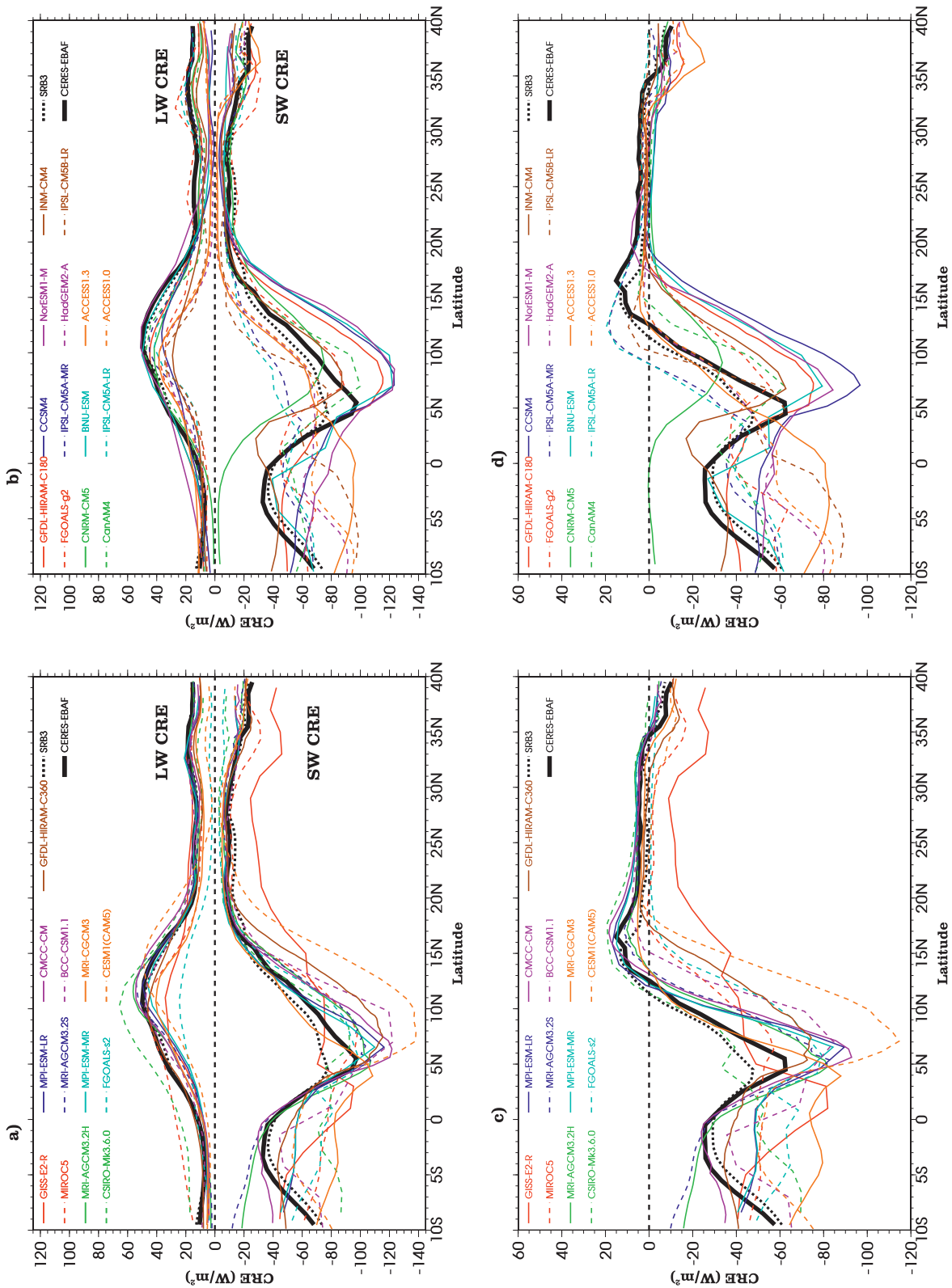


FIG. 9. (a), (b) Cloud radiative effect ($W m^{-2}$) at the top of the atmosphere in the SW (negative values) and LW (positive values) bands averaged over $10^{\circ}W-10^{\circ}E$ for the JAS period of the years 1979–2008. The left (right) panel corresponds to the warmer (colder) models over the Sahara ($20^{\circ}-30^{\circ}N, 10^{\circ}W-10^{\circ}E$). (c), (d) As in (a), (b), but for the net CRE at the top of the atmosphere.

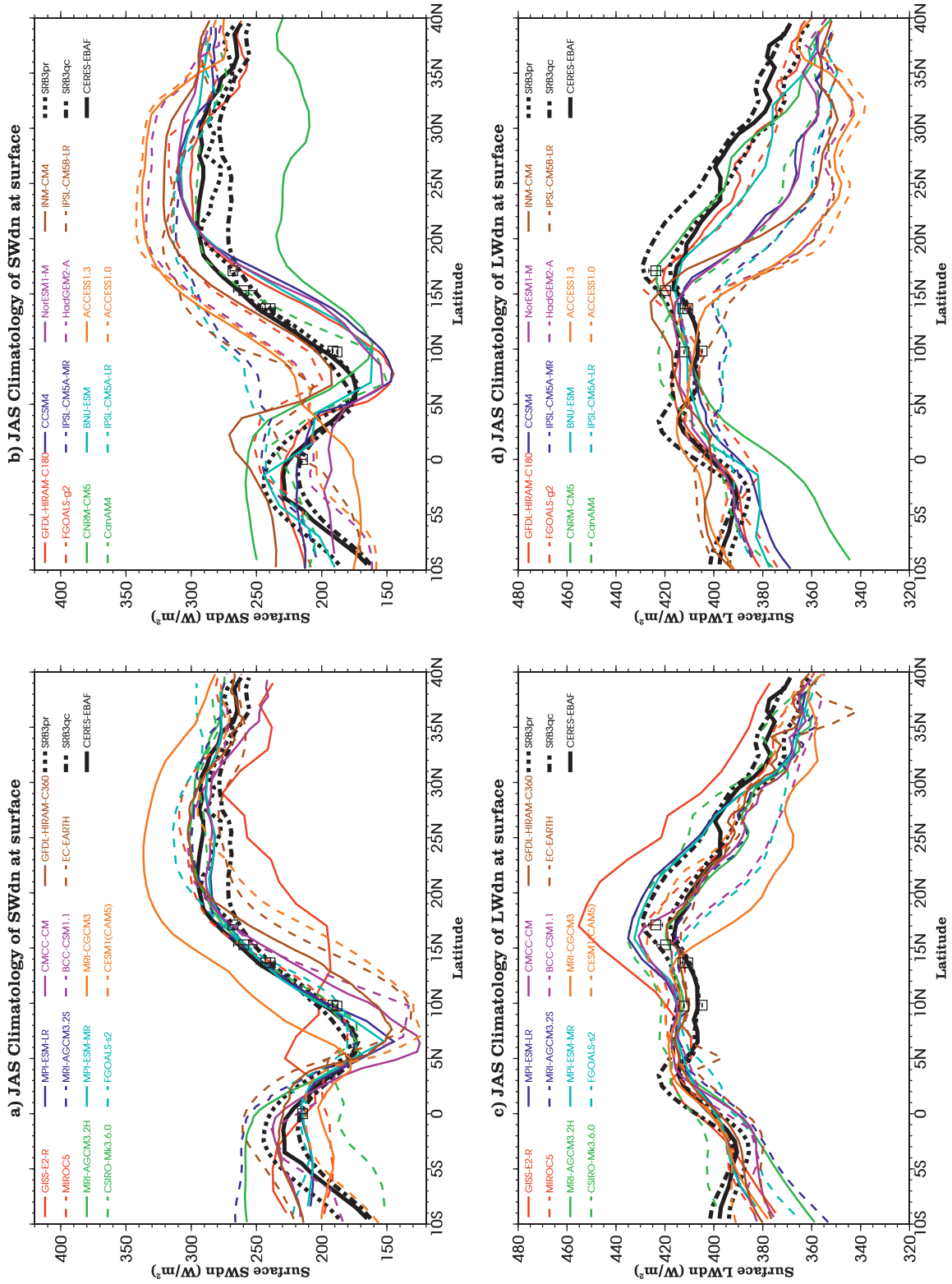


FIG. 10. As in Fig. 9, but for the downward SW and LW radiative flux at the surface. Mean fluxes for the sites along the transect (Table 3) together with their yearly minimum–maximum values are shown.

As a result, the observed net CRE is negative south of the ITCZ, where the shortwave component is dominant, and turns to slightly positive values north of the ITCZ, where the longwave component dominates. Over most of the Sahel and Sahara, midlevel and convective clouds have a positive net CRE. Thus the CRE provides locally more favorable conditions for the development of convection in the Sahel than farther south during the monsoon (Chou and Neelin 2003). Only one-half of the models capture the Sahelian band of positive net CRE, but no model reproduces accurately its meridional structure, with the right balance between the shortwave and longwave components. North of the ITCZ, the CRE is generally too small, and to the south the spread is very large.

4) INCOMING RADIATION AT THE SURFACE

Incoming radiative fluxes at the surface are important components of the surface energy budget, with the advantage that they can be reasonably evaluated with a joint utilization of in situ AMMA measurements and satellite products. Their understanding is complex as they undergo the influence of the whole troposphere thermodynamic state, the vertical distribution of cloud properties, and the aerosol loading. During the monsoon season, the latter is expected to impact less the ITCZ region as aerosols are scavenged by precipitation. However, they strongly affect the Sahara region (Knippertz and Todd 2012).

At the surface, the JAS shortwave incoming flux meridional gradient is large, reaching more than 100 W m^{-2} from the Guinean coast to the Sahara (Fig. 10) and involving a strong CRE. These variations are not accurately simulated, with JAS-mean departures from observations larger than several tens of watts per square meter. Over the Guinea coast, more than one-half of models underestimate the incoming surface shortwave flux in response to a too thin and reflective cloud layer. Within the ITCZ, the IPSL models and HadGEM2-A strongly overestimate this radiative flux. As will be shown in section 5b(2), these two models display a reasonable cloud frequency of occurrence, but they both systematically underestimate the cloud fraction (Fig. 18). Over the Sahara, most of the models overestimate the incoming surface shortwave flux, in particular the colder ones (Fig. 10b). Figure 8 pointed to a clear deficit of midlevel cloudiness, which has a strong impact in the shortwave (Bouniol et al. 2012). The representation of aerosols may also explain a large part of the spread.

Meridional fluctuations of the longwave incoming radiation at the surface are weaker. It increases from the more humid and cloudier Gulf of Guinea to the drier Sahara at 20°N by $10\text{--}20 \text{ W m}^{-2}$. Note, however, that the atmosphere warms and loads with aerosols along this direction. Several models simulate this weak gradient,

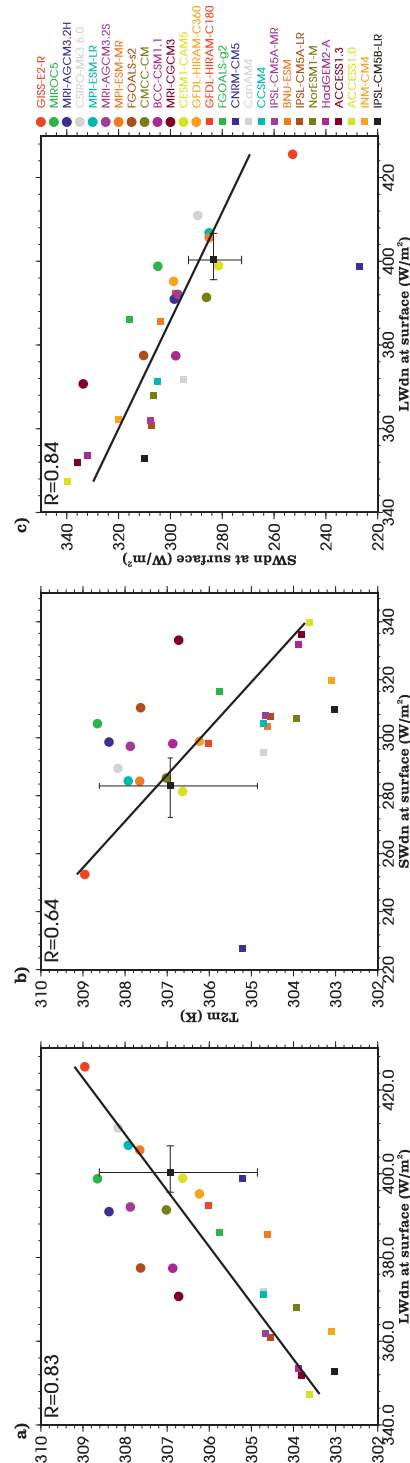


FIG. 11. (a) Scatterplot of the downward longwave radiative flux at the surface (W m^{-2}) vs the 2-m temperature (K). Both variables are averaged over ($20^\circ\text{--}30^\circ\text{N}$, $10^\circ\text{W}\text{--}10^\circ\text{E}$) for the JAS period for the years 1979–2008. The coefficient of determination of a linear regression is in the top-left corner. (b) As in (a), but for the downward shortwave radiative flux; the linear regression was performed without the CNRM-CM5 data. (c) As in (b), but for the downward longwave vs the shortwave radiative flux at the surface (W m^{-2}). The black square with error bars is the mean obtained from observational datasets (i.e., SRB3pr, SRB3qc, and CERES-EBAF for radiative fluxes, and ERAI, MERRA, and CFSR for the 2-m temperature). The warmer (colder) models are indicated with dots (filled square).

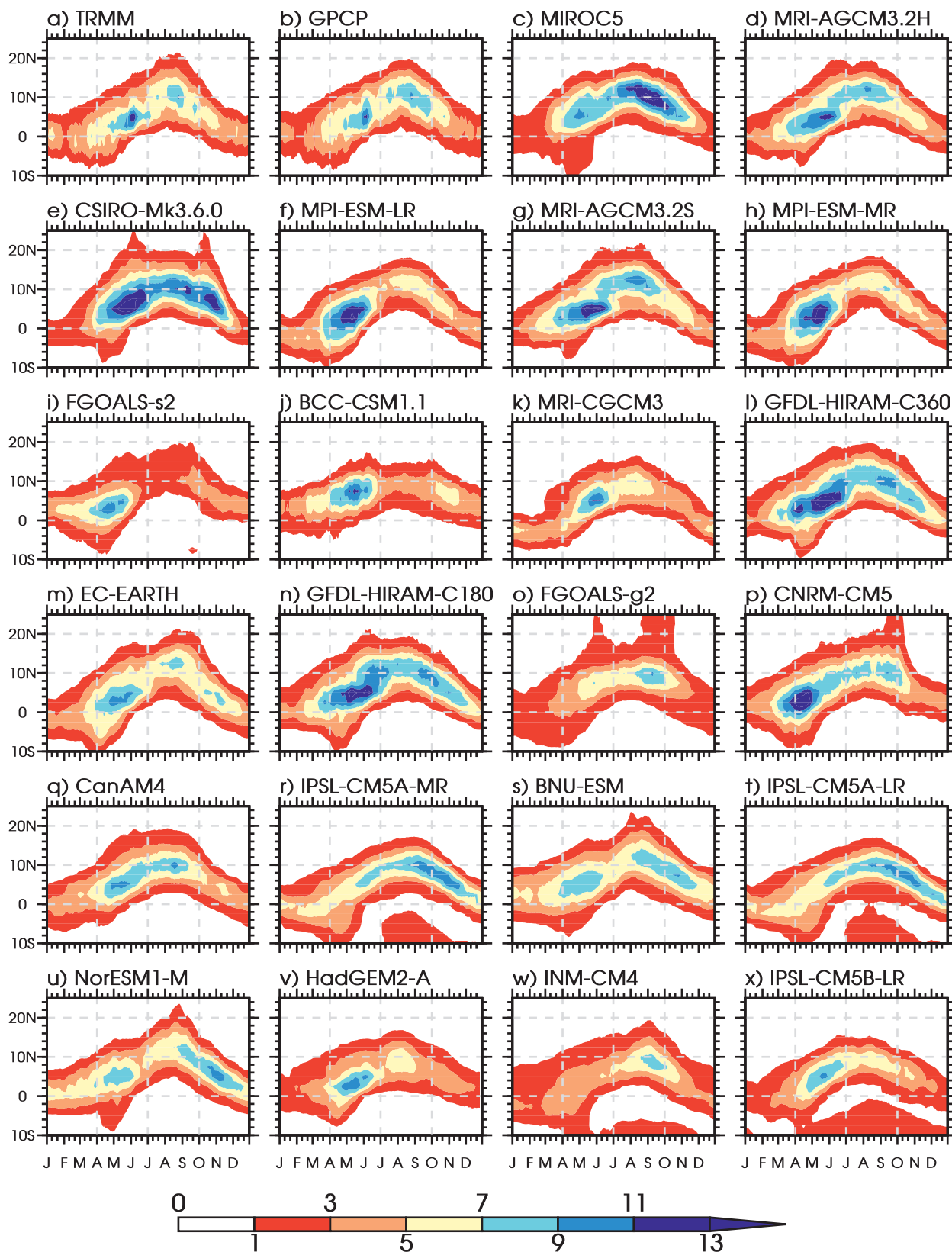


FIG. 12. Annual cycle of precipitation (mm day^{-1}) averaged over 10°W – 10°E . A 10-day running mean was used on each dataset. Models are organized (top left)–(bottom right) from the warmest one over the Sahara (20° – 30°N , 10°W – 10°E) to the coldest one.

with departures less than 20 W m^{-2} . Farther north, biases in the longwave incoming surface radiation increase significantly and reach the same order of magnitude as in the shortwave, especially in the colder models (Fig. 10d). The lack of midlevel clouds may partly explain the underestimation. Further investigations are needed to better understand the origin of the spread.

Over this dry region, feedbacks with surface air temperature are investigated in models in Fig. 11. Opposite behaviors are noted with increase (decrease) in the temperature as the longwave (shortwave) increases with a higher correlation in the longwave domain. Figure 11c shows that the higher the incoming shortwave, the lower the incoming longwave. Since most models simulate a cloud-free troposphere in a relative dry environment, this suggests important roles of the surface albedo and of the aerosol loading (Kothe and Ahrens 2010) in the spread over the Sahara. Radiative transfer calculations would help in better identifying the sources of discrepancies between models over the region.

c. *The annual cycle of the WAM*

At the seasonal time scale, the West African monsoon is characterized by a northward migration of the ITCZ with an abrupt climatological shift in early summer (Sultan and Janicot 2000, 2003), culminating in August, and by a smoother southward withdrawal of the rainfall band in September and October. The monsoon onset time is consistent in the two observational datasets (Figs. 12a,b). It is well marked by a transition between a maximum of precipitation along the Guinean coast in May–June and a second one centered near 12°N in August. In between, a minimum of rainfall occurs over the whole region as the ITCZ moves northward. Presumably because the monsoon is primarily forced by the annual excursion of the sun, most models capture the ITCZ summer migration, although with varying degrees of accuracy. Four models do not reproduce the spring precipitation maximum near the Guinea coast (FGOALS-g2, INM-CM4, IPSL-CM5A-LR and -MR), while six overestimate it (CNRM-CM5, CSIRO-Mk3.6.0, GFDL-HIRAM-C180 and -C360, MPI-ESM-LR and -MR). The monsoon is almost nonexistent in BCC-CSM1.1, very weak in FGOALS-s2, and rather weak in HadGEM2-A, IPSL-CM5B-LR, MPI-ESM-LR and -MR, and MRI-CGCM3, consistently with Fig. 6. When simulated, the onset occurs at approximately the correct time of the year, as in CNRM-CM5, CSIRO-Mk3.6.0, the two versions of GFDL-HIRAM, the two versions of MPI-ESM, and NorESM1-M. For three models (CNRM-CM5, CSIRO-Mk3.6.0, and FGOALS-g2), the 1-mm isohyet reaches latitudes above 20°N , which is observed neither in TRMM nor in GPCP. Conversely, four models simulate rain

over the Gulf of Guinea south of 0°N during the summer (INM-CM4, IPSLCM5A-LR, IPSL-CM5A-MR, and IPSL-CM5B-LR).

The annual cycle of temperature over West Africa is also characterized by a northward migration of the temperature maximum during spring and summer and a southward retreat at the end of August (Ramel et al. 2006). Two annual maxima can be identified (Fig. 13a). The first one occurs over the Sahel during May–June, prior to the monsoon rainfall onset, when the soil is still very dry, and typically at the time of the establishment of a humid low-level monsoon flow in the Sahel (Slingo et al. 2009; Guichard et al. 2009). Then, the summer rainfall over the Sahel leads to enhanced surface evapotranspiration (Timouk et al. 2009) and to an overall cooling at the surface. The second maximum occurs over the Sahara, near 27° – 28°N at the end of July, one month after the insolation maximum.

The annual cycle depicted by the CRU, European Centre for Medium-Range Weather Forecasts (ECMWF) Interim Re-Analysis (ERA-Interim), and Modern-Era Retrospective Analysis for Research and Applications (MERRA; not shown) datasets is very consistent. It is noticeable that the National Centers for Environmental Prediction (NCEP) Climate Forecast System Reanalysis (CFSR) is generally colder by 2 K over the Sahel (not shown). This perhaps surprising result is nevertheless fully consistent with recent comparisons performed over land (Wang et al. 2011; Bao and Zhang 2012).

Very large spread is found among AMIP simulations all year long. They are particularly pronounced outside of the monsoon summer season. Although most of the models simulate the northward displacement of maximum temperature from winter to summer, the spread over the Sahel reaches up to 6 K in winter and none of them captures the spring maximum over the Sahel, except to some extent BNU-ESM and HadGEM2-A. In half of the models, the amplitude of the temperature annual cycle is lower than in CRU. Some models such as BCC-CSM1.1, HadGEM2-A, INM-CM4, the IPSL-CM5 models, and MRI-CGCM3 do not form a strong heat low over the Sahara, which is consistent with an ITCZ that fails in migrating northward during the summer (Fig. 12).

5. Toward a physical evaluation of the WAM in AMIP simulations

The previous section addressed basic large-scale features of the West African monsoon. Higher-frequency fluctuations and finer-scale processes are now evaluated. These scales are indeed crucial to improve food management and disaster mitigation in the region (e.g., Sultan et al. 2005), and their evolution in the climate

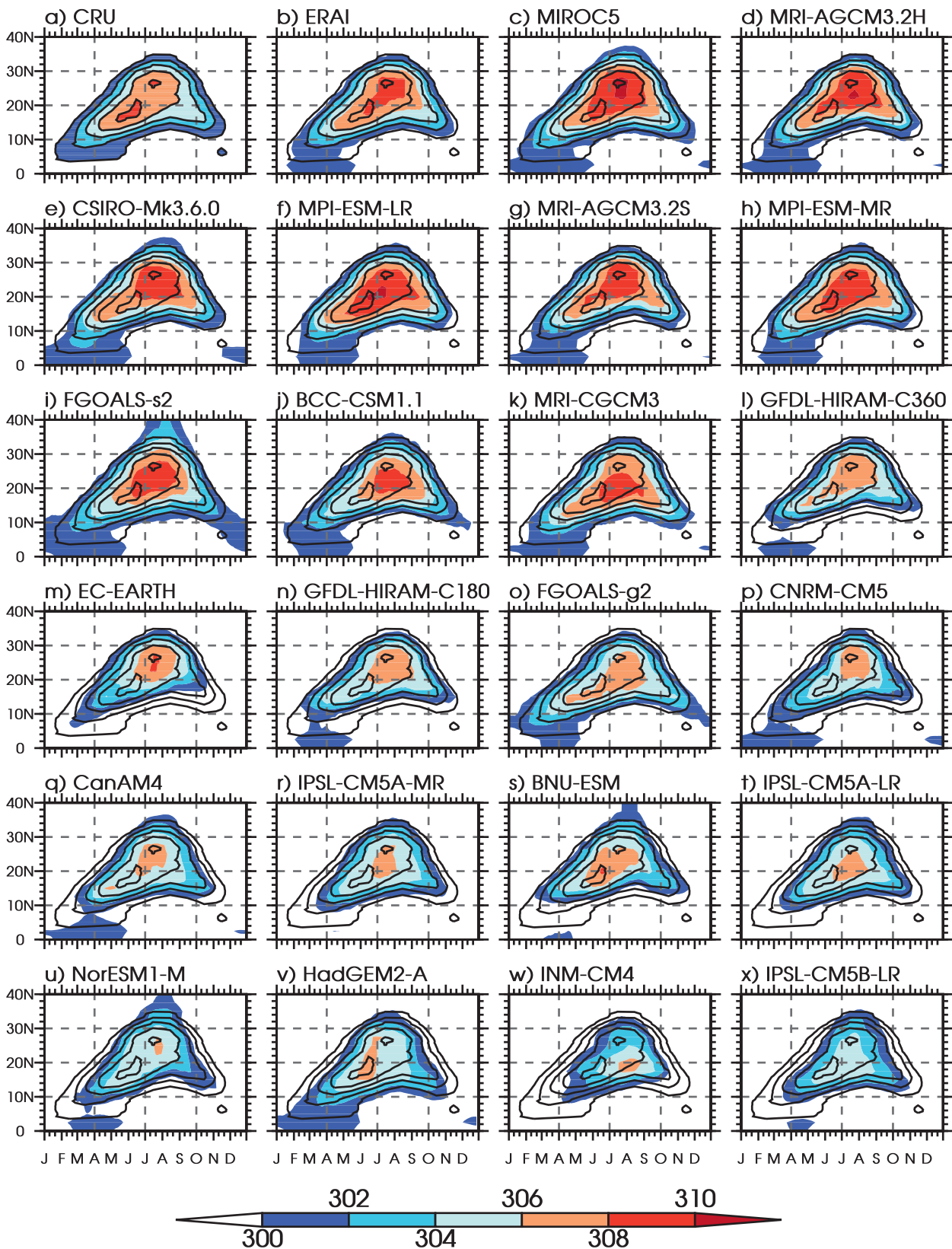


FIG. 13. As in Fig. 12, but for 2-m temperature (K).

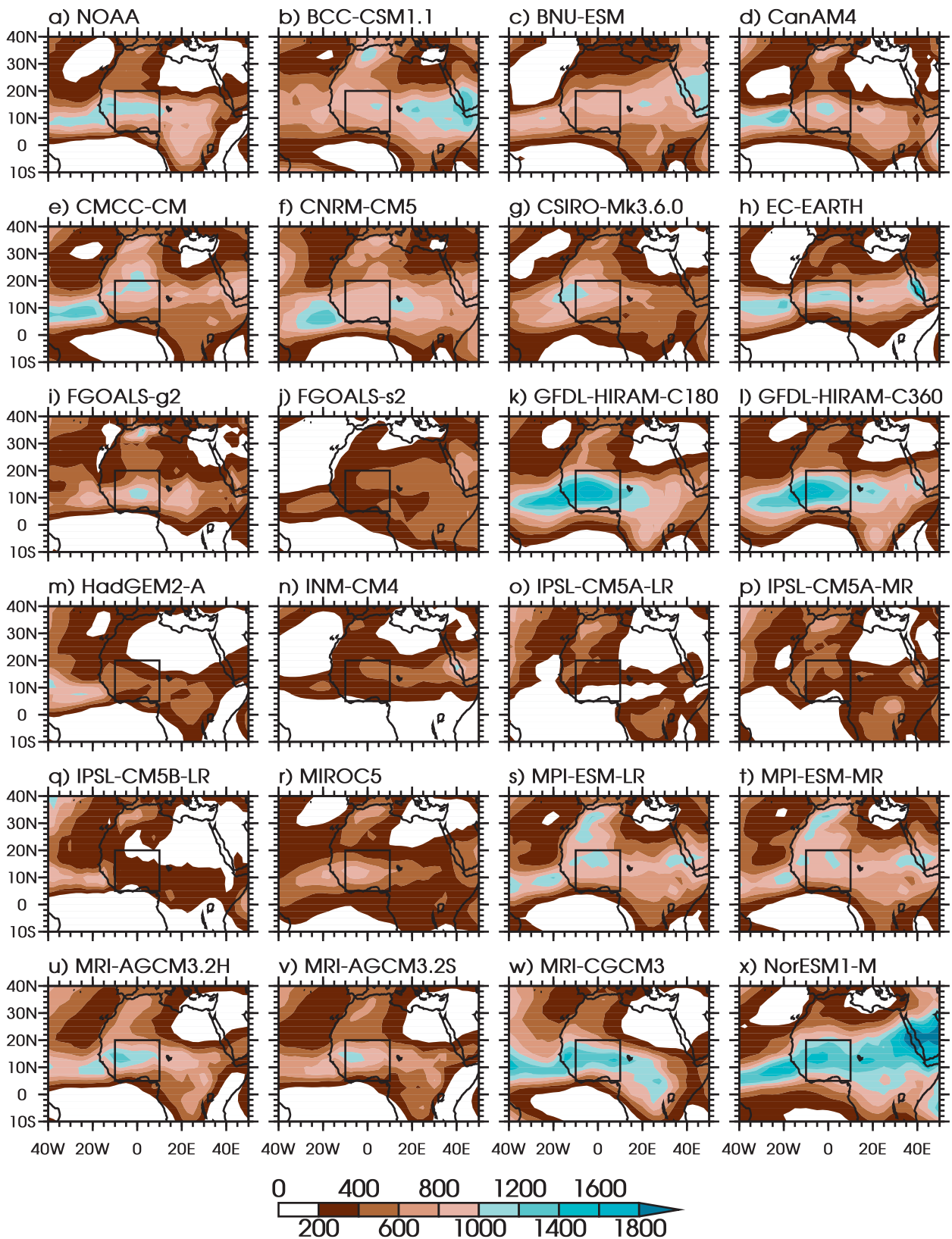


FIG. 14. Variance of OLR in the 1–90-day band ($W^2 m^{-4}$) for the JAS season from 1979 to 2008. The daily OLR of the CMIP5 models was regridded onto the National Oceanic and Atmospheric Administration (NOAA) OLR grid ($2.5^\circ \times 2.5^\circ$), before computing filtered anomalies and their variance.

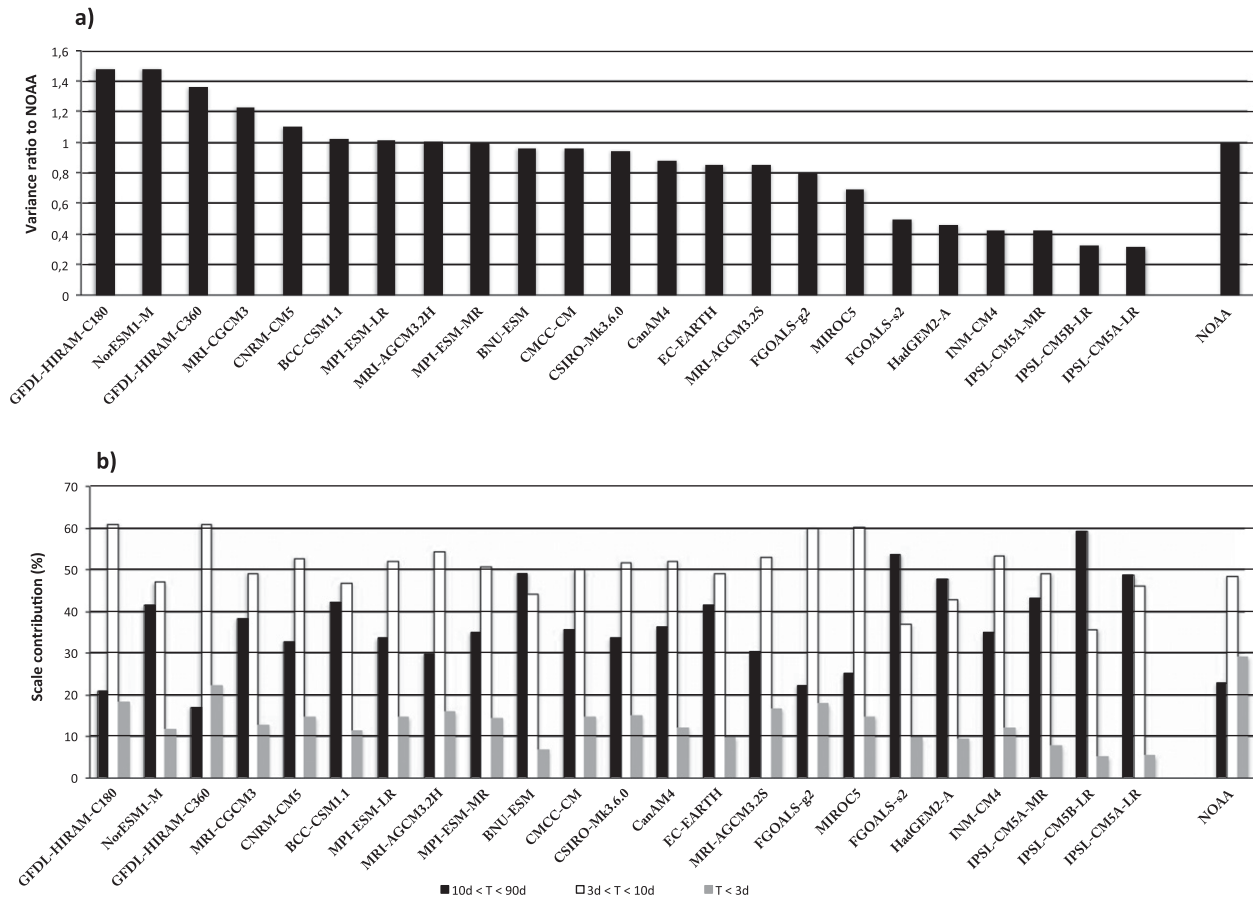


FIG. 15. (a) Variance of OLR in the 1–90-day band averaged over the domain (5° – 20° N, 10° W– 10° E) for the JAS season from 1979 to 2008. Values are normalized by the NOAA OLR variance. (b) Distribution of the OLR intraseasonal variance (%) across the 1–3-day (gray bars), 3–10-day (white bars), and 10–90-day (black bars) time scales.

change perspective is key for adaptation policies. Their representation by state-of-the-art climate models is a major target if they are to be trustworthy for simulating either present-day climate or the impact of global warming over West Africa.

a. Intraseasonal variability of precipitation

Rainfall over West Africa is highly intermittent in space and time. The rainy season is punctuated by dry and wet periods occurring at various intraseasonal time scales (Janicot et al. 2011). Three preferred time scales have been highlighted: around 40 days, probably involving the Madden–Julian oscillation (Mathews 2004; Janicot et al. 2009); approximately 15 days with two main regional modes (Mounier and Janicot 2004; Mounier et al. 2008; Janicot et al. 2010; Roehrig et al. 2011); and in the 3–10-day range with the well-known African easterly waves (AEWs; e.g., Kiladis et al. 2006). In the present study, we do not address specifically each of these intraseasonal scales. In contrast, we give a brief

overview of the main properties of convection at intraseasonal time scales, which, from this perspective, makes West Africa a unique place in the world.

Figure 14 indicates the variance of outgoing longwave radiation (OLR) filtered in the 1–90-day range. OLR is preferred to precipitation here because precipitation variance is closely related to its mean value, so that differences in precipitation variance in models are mainly attributed to bias in precipitation mean state. A zonally elongated maximum of OLR variance ($>1000 \text{ W}^2 \text{ m}^{-4}$) is observed over the Sahel, along the northern side of the ITCZ. When reaching the Atlantic Ocean, the band moves southward, up to 10° N. Intraseasonal variance is slightly weaker ($900 \text{ W}^2 \text{ m}^{-4}$) over the eastern Sahel and central Africa. Very few models capture the observed structure and amplitude over the Sahel. GFDL-HIRAM-C180 and -C360, MRI-CGCM3, and NorESM1-M overestimate the amount of intraseasonal variability, with a maximum rather collocated within the ITCZ. The southward slope in the east–west direction is

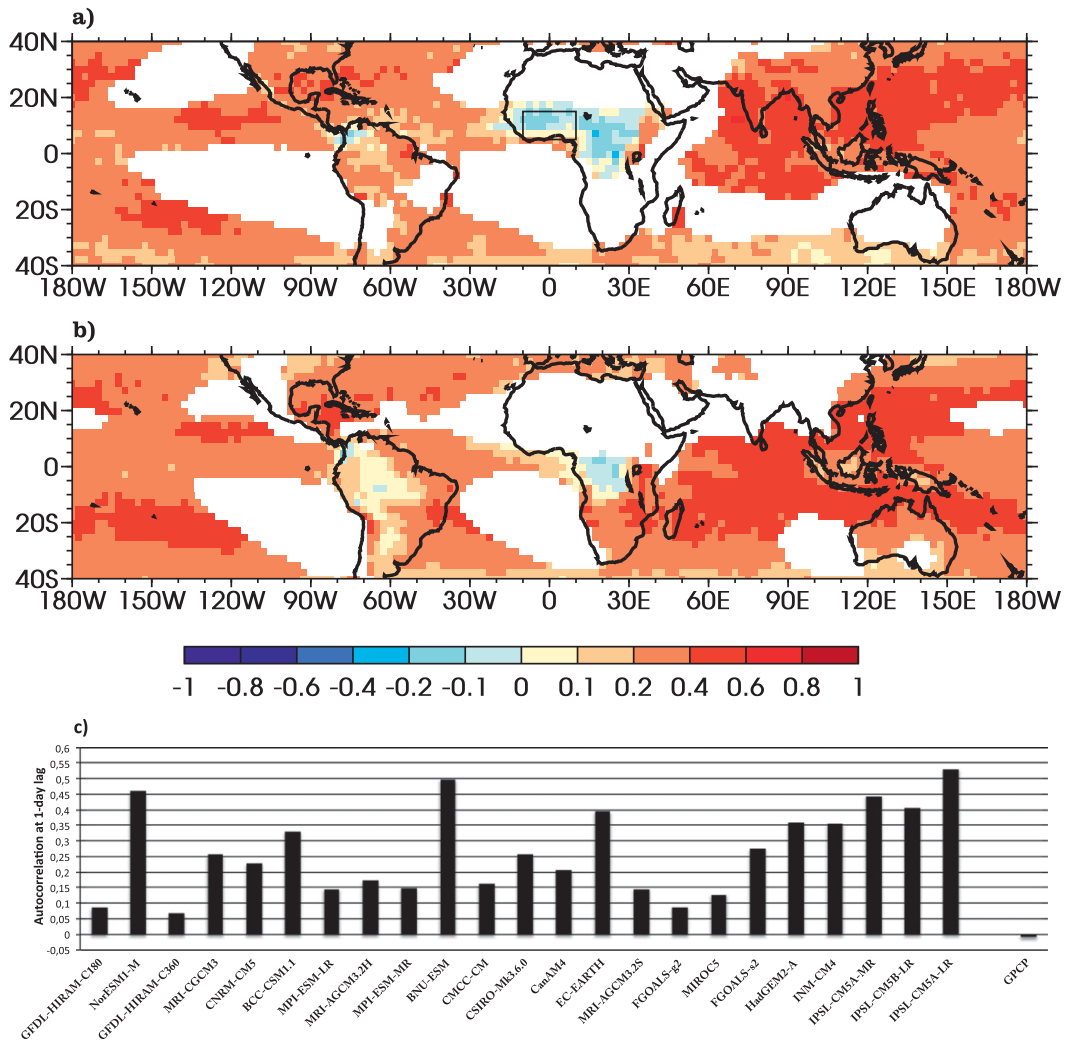


FIG. 16. Autocorrelation of (a) JAS and (b) December–February (DJF) 1–90-day filtered precipitation at a 1-day lag for the GPCP daily dataset. Only grid points where the mean precipitation was $>1 \text{ mm day}^{-1}$ were considered. (c) Autocorrelation of 1–90-day filtered precipitation at a 1-day lag for GPCP and CMIP5 models averaged over the domain ($5^{\circ}\text{--}15^{\circ}\text{N}$, $10^{\circ}\text{W--}10^{\circ}\text{E}$). Autocorrelation was computed for each JAS season for 1997–2008 for GPCP and 1979–2008 for CMIP5 model, and then averaged over all years. CMIP5 models and the GPCP dataset were regridded on the NOAA OLR grid before any computations.

generally reproduced. However, about one-half of CMIP5 models underestimate the intraseasonal variability of deep convection. Some of them have a variance reaching one-third of that observed, when averaged over the domain ($5^{\circ}\text{--}20^{\circ}\text{N}$, $10^{\circ}\text{W--}10^{\circ}\text{E}$) (Fig. 15a). These results are very similar to those obtained with the CMIP3 models (Roehrig 2010).

The observed distribution of the OLR intraseasonal variance is captured by none of the models (Fig. 15b). The 10–90-day scale (black bars) explains 20% of the intraseasonal variability in only four models (GFDL-HIRAM-C180 and -C360, FGOALS-g2, and MIROC5), while it is overestimated by more than 10% in the others. Overall,

models with underestimation of OLR intraseasonal variance put too much weight on long time scales. The 3–10-day synoptic time scale (white bars) corresponds to about 50% of the observed intraseasonal variance. All models reproduce this amount at an accuracy of $\pm 10\%$, indicating that they are likely able to simulate AEW-like variability (Ruti and Dell’Aquila 2010). However, even though convection can be organized at the synoptic or intraseasonal scales, most of summer rainfall over West Africa is provided by a very few heavily precipitating mesoscale convective systems (Mathon et al. 2002). As a consequence, precipitation is highly intermittent from day to day and has very little persistence over the Sahel. Consistent with

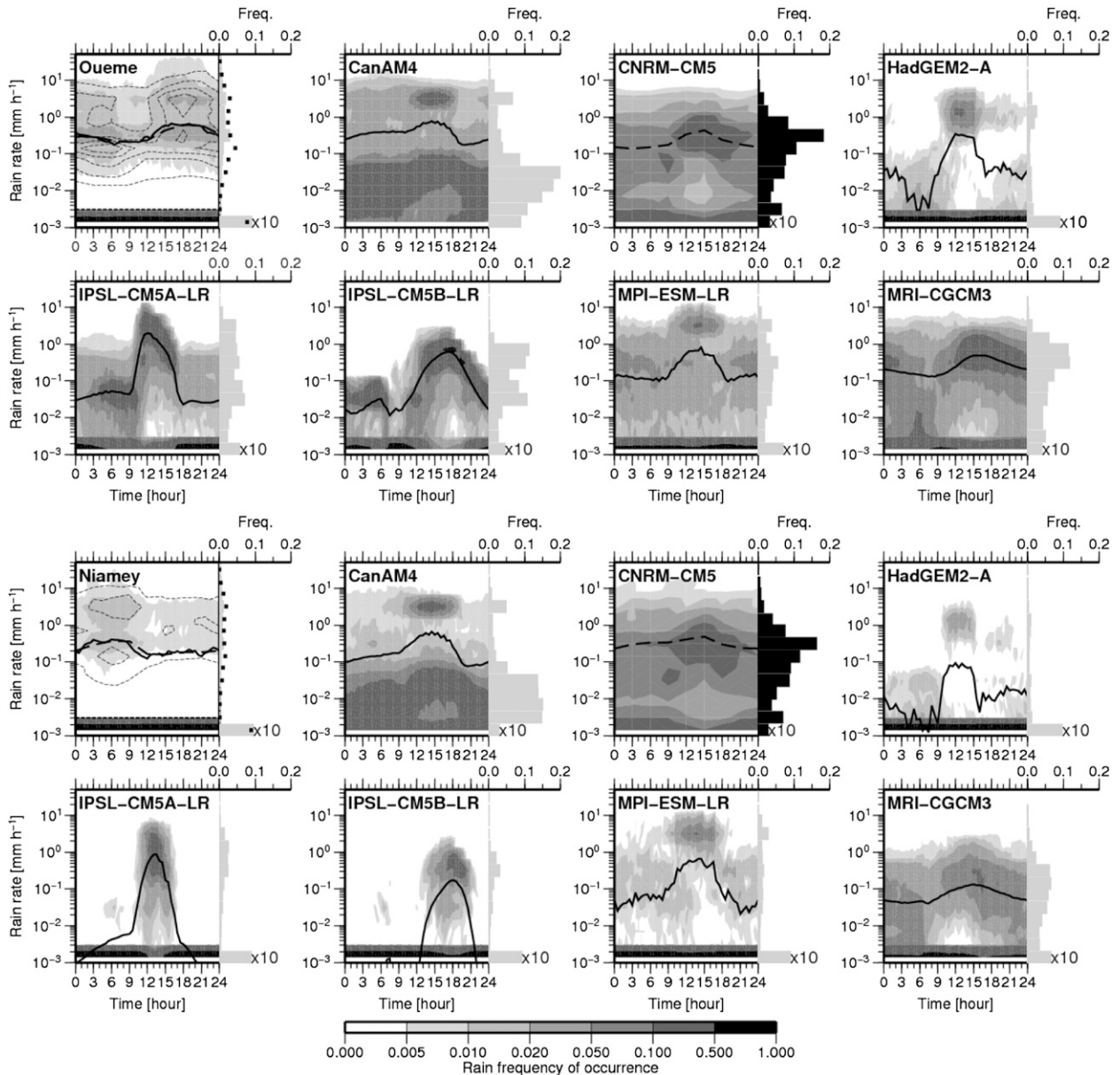


FIG. 17. Mean August diurnal cycle of precipitation intensity distribution (including null values). Periods used are 1979–2008 for the models, 1999–2011 for the Ouémé site (9.5°N , 2°E), and 1989–2011 for the Niamey site (13.5°N , 2.2°E). The distribution is based on 30-min samples. The mean diurnal cycle of rainfall intensity is superimposed (black line). The diurnal cycle of precipitation intensity distribution is also shown (dashed lines) but using 3-hourly samples for comparison with the CNRM-CM5 model.

the fact that models have difficulties to represent such convective systems [see also section 5b(1)], none of them captures the very high-frequency (1–3 days, gray bars) proportion of almost 30%. Even the high-resolution GFDL-HIRAM-C180 and -C360 runs reach only 20% in this band.

This notion of persistence can be quantitatively characterized by the autocorrelation function of precipitation. Using it, Lin et al. (2006) showed that the Madden–Julian oscillation variance in most of CMIP3 models comes

from an over-reddened spectrum, associated with too strong persistence of equatorial precipitation. In that regard, rainfall over Africa has relatively unique properties. There, precipitation at the $2.5^{\circ} \times 2.5^{\circ}$ gridpoint scale is very similar to a white noise, with a 1-day lag autocorrelation even slightly negative in some places (Fig. 16a). There is no persistence at all at the local scale. No region around the world behaves similarly, either in boreal summer (Fig. 16a) or in boreal winter (Fig. 16b), except to some extent the northern part of South America. Figure

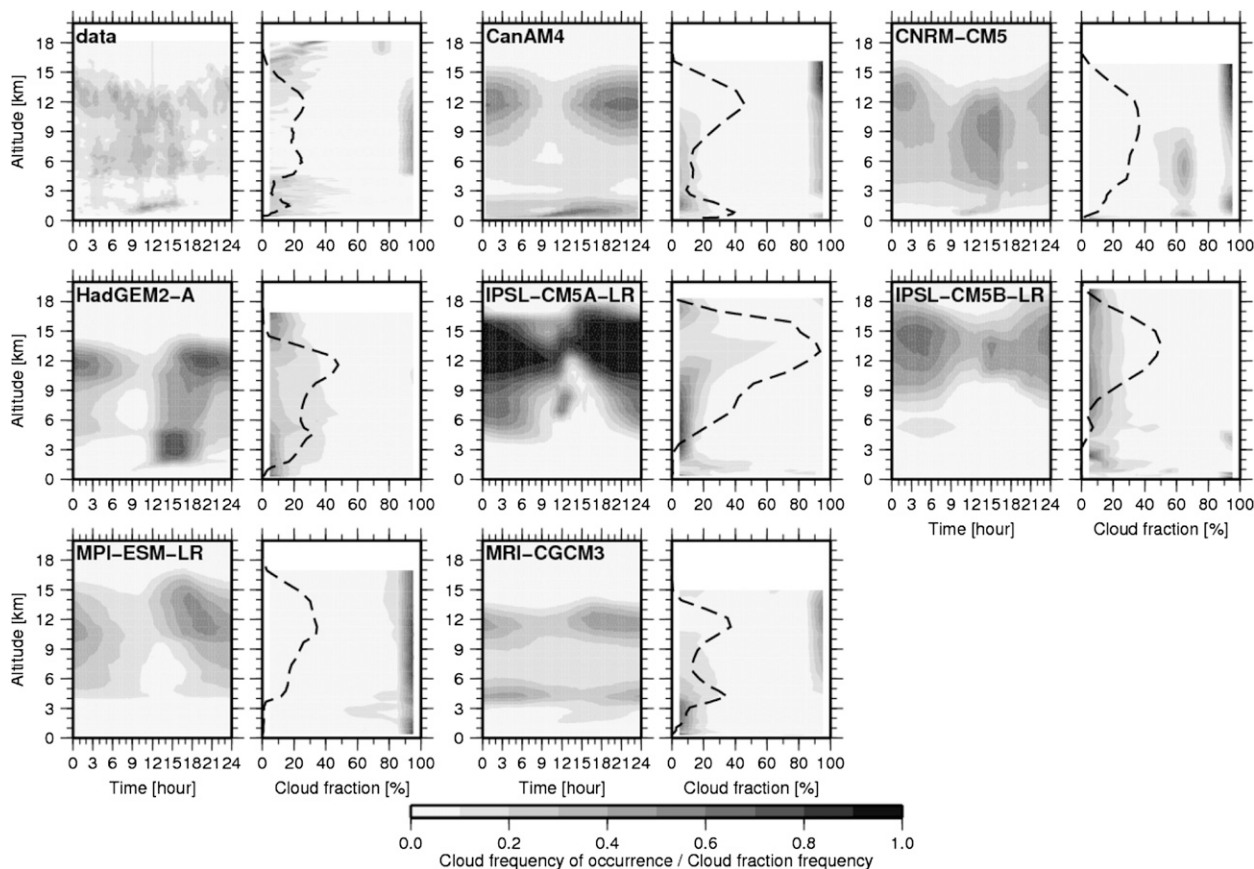


FIG. 18. As in Fig. 17, but for the August diurnal cycle of the cloud frequency of occurrence derived at the Niamey site (13.5°N, 2.2°E). Observations come from the AMF data acquired in 2006. The period 1979–2008 is used for the models. The vertical distribution of the cloud fraction is indicated in the right subpanels. It is normalized at each level by the total cloud frequency of occurrence (dashed line.)

16c confirms that such a property of the West African monsoon remains a challenge for most of state-of-the-art models. GFDL-HIRAM-C360 reaches the closest value to zero (0.06), and is closely followed by GFDL-HIRAM-C180 (0.09), FGOALS-g2 (0.09), and MIROC5 (0.12).

The relative success of the GFDL-HIRAM models might be partly attributed to their high spatial resolution. The correct behavior of MIROC5 is possibly related to the effort undertaken to make the convective scheme more sensitive to dry air in the free troposphere (Chikira and Sugiyama 2010), and which eliminates the artificial triggering function¹ for deep convection used in the previous version (CMIP3) of the MIROC model and based on the work of Emori et al. (2001). In CMIP3, MIROC3.2(medres) and MIROC3.2(hires) had a similar behavior to

MIROC5 with regards to this diagnostic (Roehrig 2010). The CMIP3 MRI model (MRI CGCM2.3.2a), which was sharing the same convective parameterization (Pan and Randall 1998) except for this artificial triggering, produced too much persistence of precipitation over West Africa.

b. The diurnal cycle at selected AMMA sites

The CMIP5 archive contains for a few AMIP simulations a large set of diagnostics at high temporal frequency, for 10 grid points along the West African transect. This high-frequency output allows us to evaluate finescale processes.

1) PRECIPITATION

Rain over West Africa is mainly of convective origin (Mathon et al. 2002). Convective system properties (size, life cycle, and organization) strongly depend on latitude, leading to different characteristics of the diurnal cycle of precipitation. Figure 17 illustrates such differences

¹The triggering of deep convection occurred only when the relative humidity averaged over the vertical went over a given threshold (~80%).

between two sites distant from less than 500 km in the north–south direction: the Ouémé site (9.5°N), just along the southern fringe of the ITCZ, and the Niamey site (13.5°N). The southernmost site presents a bimodal diurnal cycle with a first peak around 1800 UTC and a smaller one between 0300 and 0600 UTC. Farther north, only the morning peak remains. Over Niamey, about 80% of the annual rainfall is produced by westward propagating systems (Dhonneur 1981), initiated in the afternoon over the elevated terrain of northeastern Niger located several hundreds of kilometers eastward and reaching the Niamey region in the early morning (Rickenbach et al. 2009). South of the ITCZ, the contribution of propagating systems decreases to 50% (Fink et al. 2002; Depraetere et al. 2009), and a more common late afternoon peak arises. This bimodal structure observed here is consistent with the secondary nighttime peak emerging from global datasets (Yang et al. 2008).

To our knowledge, no model explicitly includes a proper representation of propagating mesoscale convective systems such as squall lines, so that they are not expected to capture the diurnal cycle of precipitation over Niamey. Indeed, Fig. 17 illustrates that the precipitation distribution of the models is qualitatively very similar between the two sites. The variations between the two sites are related to a more seldom occurrence of rain events at higher latitudes. This accounts for the differences in the distribution of the two IPSL models. As a consequence, the use of the Ouémé site as a reference appears more suitable for evaluating the diurnal cycle of rainfall over West Africa (Fig. 17), at least until models can properly represent propagating convective systems.

Consistent with previous studies (Betts and Jakob 2002; Guichard et al. 2004), the distribution of precipitation in CMIP5 models peaks in afternoon. A first group of models (CanAM4, CNRM-CM5, IPSL-CM5A-LR, HadGEM2-A, and MPI-ESM-LR) displays a too early peak of precipitation, between 1200 and 1500 UTC, roughly in phase with insolation. More recently, Nikulin et al. (2012) showed that the same issue affects regional climate models of the CORDEX-Africa experiments, despite their finer resolution (around 50 km). This incorrect timing of rainfall impacts on the surface water and energy budgets in various ways (Del Genio 2012).

In the two remaining models (IPSL-CM5B-LR and MRI-CGCM3), the precipitation maximum occurs later, between 1500 and 1800 UTC, more in phase with observations. The difference between IPSL-CM5A-LR and IPSL-CM5B-LR in particular attests to recent progress on this long-standing issue. Rio et al. (2013) and Sane et al. (2012) discussed this improved behavior of IPSL-CM5B-LR, which they attributed to a more

realistic description of thermal plumes in the boundary layer (Rio and Hourdin 2008), the introduction of a parameterization of convective cold pools (Grandpeix and Lafore 2010), and an improved closure and triggering for convection (Rio et al. 2013).

There is also a large spread in the amplitude and intensity of this afternoon maximum, hence affecting the distribution of rain intensity (Fig. 17). Most models have a maximum frequency of occurrence for an intensity near 1 mm h^{-1} , reaching even larger values in MPI-ESM-LR. In the remaining part of the diurnal cycle, rain intensity decreases by one to two orders of magnitude in IPSL-CM5A-LR, IPSL-CM5B-LR, HadGEM2-A, and MPI-ESM-LR, and by less than one in CanAM4, CNRM-CM5, and MRI-CGCM3. These three models simulate a substantial amount of precipitation during most of the day. In particular, rain-free periods² cover less than 8% of the time in CanAM4, 30% in CNRM-CM5, and 39% in MRI-CGCM3, compared to 89% in observations.

Despite the lack of organized convective systems in models and the differences in the rain distribution at the diurnal scale, models overall agree with observations on the JAS mean rate (Fig. 6). It can thus be argued that the climatological average arises from compensating errors similar to those stressed in Stephens et al. (2010): precipitation occurs approximately twice as often as in observations, but at rates far too weak.

2) FINESCALE PROPERTIES OF CLOUD COVER

The diurnal cycle of cloud cover impacts not only the water cycle, but also the surface energy balance, through the surface incoming shortwave flux in particular. Bouniol et al. (2012) highlighted that all cloud types present a well-marked diurnal cycle in the Sahel (Fig. 18). Two peaks of convective cloud occurrence can be identified (around 0900 and 1500 UTC), consistent with the arrival of propagating convective systems and locally initiated convection. Low-level clouds associated with the daytime growth of the boundary layer increase between 0900 and 1600 UTC. The maximum in mid-level cloud cover occurs between 0300 and 0600 UTC. Cirrus cloud cover decreases between 1200 and 1500 UTC. The distribution of cloud fraction, also displayed in Fig. 18, highlights the distinct cloud fractions associated with each cloud type: low-level and cirrus clouds are relatively broken, while midlevel and convective clouds are associated with high cloud fractions.

² Rain-free periods are defined as precipitation intensity lower than $2 \times 10^{-3} \text{ mm h}^{-1}$, since some models do not generate rain rates that exactly equal to zero.

Consistent with the diurnal cycle of precipitation, clouds associated with convection are shifted toward midday in CanAM4, CNRM-CM5, HadGEM2-A, IPSL-CM5A-LR, and MPI-ESM-LR, which induce a too early minimum high-level cloud cover. This is generally followed by a strong occurrence of deep clouds resulting from condensates detrained from convective updraft and treated in most models as a passive stratiform cloud (Del Genio 2012). However, the results are contrasted, as models overestimating rain frequency of occurrence are not necessarily those that overestimate the cloud frequency at high levels (e.g., CanAM4 and MRI-CGM3).

IPSL-CM5B-LR and MRI-CGCM3 show to some extent an improved timing of midlevel cloud occurrence, but with inaccurate frequencies of occurrence. The diurnal cycle of low-level clouds is properly represented in CNRM-CM5 and CanAM4 even if the growth of the boundary layer seems to be slightly underestimated. HadGEM2-A and MRI-CGCM3 have a very low occurrence of these clouds, and they appear much too early. MPI-ESM-LR misses this type of clouds. IPSL-CM5A-LR and IPSL-CM5B-LR also miss them at Niamey due to an ITCZ located too much southward. Both models capture them more to the south, but with a too early triggering in IPSL-CM5A-LR.

The statistics of cloud fraction associated with the various cloud types are very different from one model to another. IPSL-CM5A-LR, IPSL-CM5B-LR, and HadGEM2 simulate only broken clouds for deep and midlevel clouds, whereas only high cloud fraction values occur in MPI-ESM-LR. CNRM-CM5 has a bimodal distribution, but with an unphysical peak at 65% for the deep cloud fraction. Finally, CanAM4 and MRI-CGCM3 also present a bimodal structure, with weak cloud fraction values for low-level clouds and high cloud fraction values in the upper levels.

6. Summary and conclusions

In this paper, we present a comprehensive analysis of the representation of the West African monsoon in the recently available CMIP5 simulations of both present-day and future climates. The model behavior over the Sahel region is examined across a range of time scales, going from climate change projections and multidecadal and interannual variability to the intraseasonal and diurnal fluctuations. A specific emphasis is put on the use of a comprehensive set of observational data now available (in particular AMMA and satellite data) to evaluate the WAM representation across those scales.

CMIP5 climate change projections in surface air temperature and precipitation are found to be very similar to

those of CMIP3. A robust tendency to warming over the Sahel is noticed (about 4 K on average in the RCP8.5 scenario), larger by 10%–50% compared to the global warming. As in CMIP3, the spread of model projections remains very large for both temperature and precipitation. About 80% of models agree on a modest drying around 20% over the westernmost Sahel (15°–5°W), while about 75% of models agree on an increase of precipitation over the Sahel between 0° and 30°E, with a large spread on the amplitude. This relatively high agreement, however, might involve the deficiencies that coupled models have in simulating the Atlantic SSTs (Vizy et al. 2013). Overall, the precipitation response tends to be lower than the observed decadal variability in the second half of the twentieth century. Five outliers³ predict a rainfall increase greater than 70%, which cancels part of the Sahel warming during the summer monsoon. In contrast, two CMIP3 models predict a strong drying of the Sahel, around 40%. Further investigation on the rainfall response mechanisms in those models should help to assess their credibility. It should be noted that temperature changes also remain very uncertain and that their consequences might be as dramatic as those associated with precipitation.

CMIP5 coupled models still suffer major SST biases in the equatorial Atlantic, which induce a systematic southward shift of the ITCZ during the summer in most models, when they are compared to their AMIP counterparts. The similarity between these biases in CMIP3 and CMIP5 appeals to revisit the current strategy in climate modeling research programs.

The ability of coupled models to simulate the multidecadal and interannual variability is assessed with AMIP historical and preindustrial control runs. The decadal variability of the twentieth century is underestimated in most of the last two types of experiments. In AMIP simulations, most models capture the partial recovery of monsoon rainfall of the recent decades, consistent with the role of SSTs in forcing Sahel precipitation (Giannini et al. 2003; Biasutti et al. 2008). The AMIP time sequence, however, is too short to get rid of internal variability, and ensemble AMIP simulations should be useful for further analysis.

Because of these strong biases in coupled experiments, further evaluation is performed in SST-imposed CMIP5 simulations using the 10°W–10°E AMMA transect. Almost all of them capture the broad features of a monsoon, but with various degrees of accuracy:

³The term “outlier” indicates here models that simulate a rather different response to the main stream.

- The averaged Sahel rainfall exhibits a large spread ($\pm 50\%$).
- The dispersion in surface air temperature is large over the Sahel and Sahara, and the simulations of the Saharan heat low and monsoon latitudinal position appear to be linked. The representation of the radiative aerosol properties and surface albedo in this arid region may explain part of this spread.
- The meridional structure of cloud cover and its radiative impact are tough challenges for CMIP5 models. This leads to large biases in the surface energy balance, which are likely to feed back on the monsoon at larger scales.
- The annual cycle of temperature exhibits a wide dispersion. This points to the importance of physical processes in the seasonal dynamics of temperature, and questions some conclusions that could be drawn from models about the climate sensitivity of the phase and amplitude of the temperature annual cycle over the Sahel.
- The intermittence of precipitation over West Africa is large and only a few models reproduce it and more broadly the main features of intraseasonal variability of convection there. Results from the GFDL-HIRAM models suggest that intraseasonal variability is improved with higher resolution but not necessarily the WAM mean state.

The finescale properties of rainfall and clouds are further evaluated at selected sites, for which high-frequency physical diagnostics were provided by some CMIP5 models. It appears that the wrong phasing of the diurnal cycle of precipitation remains an issue, even though some major improvements can be noticed in two models. However, most of the precipitation over the Sahel is provided by large mesoscale propagating systems, whose representation is still a challenge.

To summarize, even if most CMIP5 models capture many features of the West African monsoon, they have not reached yet a degree of maturity that directly makes them trustable to anticipate climate changes and their impacts, especially with regard to rainfall. Although encouraging progresses have been achieved, many systematic and robust biases of the coupled and atmospheric models have not improved from CMIP3 to CMIP5. This weakens our confidence in climate projection over West Africa, and even beyond over remote regions such as the Pacific (e.g., Ding et al. 2012). A large program aiming to address these systematic biases needs to be designed by the research community, under the umbrella of international programs. The observational datasets, acquired with AMMA and more recent programs such as Fennec (Washington et al. 2012), should be a backbone of these efforts.

The results of the present study point to the need to separate as much as possible the issues related to slow

and fast physical processes. Many systematic errors appear rapidly and could be addressed with numerous short-duration numerical experiments based on observed case studies and high-resolution modeling results. An example of such an approach is the Transpose-AMIP protocol, which appears as a promising tool to understand the physics of systematic atmospheric model biases (Williams et al. 2013, and reference therein). The analysis of short-term initialized coupled simulations may also provide an interesting framework to better understand SST biases in the tropical Atlantic (Huang et al. 2007; Vannière et al. 2013). For issues related to slow physics, it is further necessary to distinguish those related to remote and regional mechanisms. Regional models and regionally nudged global models seem to be the best tool to separate them (Joly and Voltaire 2009; Pohl and Douville 2011). Large surface radiative biases in arid and semiarid regions are a major issue in current simulations. They lead to departure from the observed radiative balance. The surface albedo and the representation of aerosols and their radiative properties request dedicated numerical sensitivity experiments with common protocols.

The present study not only focuses on the West African monsoon basic state in CMIP5 simulations (e.g., the precipitation seasonal amount) but also contributes to the evaluation of the rainfall distribution along the summer season (e.g., intraseasonal variability). The good representation of this rainfall distribution is crucial for the analysis of agricultural yields, biomass, and water resources. There is a need to further evaluate the ability of current models to represent and predict rainfall properties at these short time (and space) scales, including the monsoon onset and retreat, as well as dry and wet spells.

Acknowledgments. Based on a French initiative, AMMA was built by an international scientific group and is currently funded by a large number of agencies, especially from France, the United Kingdom, the United States, and Africa, and by a European Union program. Detailed information on scientific coordination and funding is available on the AMMA International web site <http://www.amma-international.org>.

We wish particularly to thank the principal investigators who make the various AMMA-CATCH ground-based measurements data sets available to the AMMA data base: S. Galle, C. Lloyd, B. Cappelaere, F. Timouk, and L. Kergoat for the surface radiation measurements, and T. Vischel, M. Gosset, G. Quantin, and E. Mougin for the rain gauge network measurements.

The PIRATA buoy measurements were provided by TAO Project Office of NOAA/PMEL.

The Niamey AMF data were obtained from the Atmospheric Radiation Measurement (ARM) Program

Archive of the U.S. Department of Energy. *CloudSat* data were obtained from CIRA of Colorado State University. ICARE and NASA gave access to the CALIOP data. The SRB and CERES data were obtained from the NASA Langley Research Center Atmospheric Sciences Data Center. CMAP Precipitation and Interpolated OLR data were provided by the NOAA/OAR/ESRL PSD, Boulder, Colorado, USA, from their Web site at <http://www.esrl.noaa.gov/psd/>. The CRU dataset was provided by the British Atmospheric Data Centre (BADC), from their Web site at <http://badc.nerc.ac.uk>. The GPCP 1DD and TRMM 3B42 data were provided by the NASA/Goddard Space Flight Center's Mesoscale Atmospheric Processes Laboratory, which develops and computes the 1DD as a contribution to the GEWEX Global Precipitation Climatology Project and the 3B42 as a contribution to TRMM. The CFSR data were developed by NOAA's National Centers for Environmental Prediction (NCEP) and were obtained from the NOAA's National Operational Model Archive and Distribution System (NOMADS), which is maintained at NOAA's National Climatic Data Center (NCDC). The MERRA data were acquired from the Goddard Earth Sciences (GES) Data and Information Services Center (DISC; <http://disc.sci.gsfc.nasa.gov>). ERA-Interim data were obtained from the ECMWF Data Server.

We acknowledge the World Climate Research Programme's Working Group on Coupled Modelling, which is responsible for CMIP, and we thank the climate modeling groups (listed in Table 1 of this paper) for producing and making available their model output. For CMIP, the U.S. Department of Energy's Program for Climate Model Diagnosis and Intercomparison provides coordinating support and led development of software infrastructure in partnership with the Global Organization for Earth System Science Portals.

F. Favot and S. Tyteca are greatly acknowledged for their support. We also acknowledge the support of the IPSL data center CICALAD and the IPSL distribution platform PRODIGUER for providing us access to their computing resources and data.

Finally, we acknowledge the thoughtful comments of Edward Vizy and one anonymous reviewer, which clearly helped to clarify and improve the manuscript.

R. Roehrig acknowledges financial support from the European Commission's 7th Framework Programme, under Grant Agreement 282672, EMBRACE project. D. Bouniol and F. Guichard were financially supported by CNES and the EUCLIPSE project from the European Union, Seventh Framework Programme (FP7/2007–2013) under grant agreement 244067. F. Guichard and F. Hourdin acknowledge financial support from the ESCAPE program (ANR-10-CEPL-005).

APPENDIX

Model Expansions

ACCESS1.0	Australian Community Climate and Earth System Simulator version 1.0
ACCESS1.3	Australian Community Climate and Earth System Simulator version 1.3
BCC-CSM1.1	Beijing Climate Center, Climate System Model, version 1.1
BCC-CSM1.1(m)	Beijing Climate Center, Climate System Model, version 1.1, with moderate resolution
BNU-ESM	Beijing Normal University—Earth System Model
CanAM4	Canadian Atmospheric Model, version 4
CanCM4	Canadian Coupled Model, version 4
CanESM2	Canadian Earth System Model, version 2
CCSM4	Community Climate System Model, version 4
CESM1(BGC)	Community Earth System Model, version 1, with Biogeochemistry
CESM1(CAM5)	Community Earth System Model, version 1, with Community Atmospheric Model, version 5
CESM1(FASTCHEM)	Community Earth System Model, version 1, with superfast chemistry
CESM1(WACCM)	Community Earth System Model, version 1—Whole Atmosphere Community Climate Model
CMCC-CM	Centro Euro-Mediterraneo per I Cambiamenti Climatici Climate Model
CMCC-CMS	Centro Euro-Mediterraneo per I Cambiamenti Climatici Climate Model, with a well-resolved stratosphere
CMCC-ESM	Centro Euro-Mediterraneo per I Cambiamenti Climatici Earth System Model
CNRM-CM5	Centre National de Recherches Météorologiques Coupled Global Climate Model, version 5

CSIRO-Mk3.6.0	Commonwealth Scientific and Industrial Research Organisation Mark, version 3.6.0
EC-EARTH	European Consortium-Earth Model
FGOALS-g2	Flexible Global Ocean-Atmosphere-Land System Model, grid point version 2
FGOALS-s2	Flexible Global Ocean-Atmosphere-Land System Model, spectral version 2
FIO-ESM	The First Institute of Oceanography Earth System Model
GFDL-CM2p1	Geophysical Fluid Dynamics Laboratory Climate Model version 2.1
GFDL-CM3	Geophysical Fluid Dynamics Laboratory Climate Model version 3
GFDL-ESM2G	Geophysical Fluid Dynamics Laboratory Earth Science Model 2 with Generalized Ocean Layer Dynamics (GOLD) ocean model
GFDL-ESM2M	Geophysical Fluid Dynamics Laboratory Earth Science Model 2 with Modular Ocean Model (MOM), version 4.1
GFDL-HIRAM-C180	Geophysical Fluid Dynamics Laboratory High Resolution Atmospheric Model C180
GFDL-HIRAM-C360	Geophysical Fluid Dynamics Laboratory High Resolution Atmospheric Model C360
GISS-E2-H	Goddard Institute for Space Studies Atmospheric Model E, version 2, coupled with the Hybrid Coordinate Ocean Model (HyCOM)
GISS-E2-H-CC	Goddard Institute for Space Studies Model E, version 2, coupled with HyCOM, carbon cycle
GISS-E2-R	Goddard Institute for Space Studies Model E, version 2, coupled with Russell ocean model
GISS-E2-R-CC	Goddard Institute for Space Studies Model E, version 2, coupled with Russell ocean model, with carbon cycle
HadCM3	Third climate configuration of the Met Office Unified Model
HadGEM2-A	Hadley Centre Global Environmental Model 2, atmosphere only
HadGEM2-AO	Hadley Centre Global Environmental Model 2, coupled atmosphere–ocean
HadGEM2-CC	Hadley Centre Global Environmental Model 2, with carbon cycle
HadGEM2-ES	Hadley Centre Global Environmental Model 2, Earth System
INM-CM4	Institute of Numerical Mathematics Coupled Model, version 4.0
IPSL-CM5A-LR	L’Institut Pierre-Simon Laplace Coupled Model, version 5A, low resolution
IPSL-CM5A-MR	L’Institut Pierre-Simon Laplace Coupled Model, version 5A, medium resolution
IPSL-CM5B-LR	L’Institut Pierre-Simon Laplace Coupled Model, version 5B, low resolution
MIROC4h	Model for Interdisciplinary Research on Climate, version 4, high resolution
MIROC5	Model for Interdisciplinary Research on Climate, version 5
MIROC-ESM	Model for Interdisciplinary Research on Climate Earth System Model
MIROC-ESM-CHEM	Model for Interdisciplinary Research on Climate Earth System Model, chemistry coupled version
MPI-ESM-LR	Max Planck Institute Earth System Model, low resolution
MPI-ESM-MR	Max Planck Institute Earth System Model, medium resolution
MPI-ESM-P	Max Planck Institute Earth System Model, low resolution and paleo mode
MRI-AGCM3.2H	Meteorological Research Institute Atmospheric General Circulation Model, version 3.2 (60 km resolution)
MRI-AGCM3.2S	Meteorological Research Institute Atmospheric General Circulation Model, version 3.2 (20 km resolution)
MRI-CGCM3	Meteorological Research Institute Coupled General Circulation Model, version 3
NorESM1-M	Norwegian Earth System Model, version 1, intermediate resolution
NorESM1-ME	Norwegian Earth System Model, version 1, intermediate resolution, with prognostic biogeochemical cycling

REFERENCES

- Bao, X., and F. Zhang, 2012: Evaluation of NCEP/CFSR, NCEP/NCAR, ERA-Interim, and ERA-40 reanalysis datasets against independent sounding observations over the Tibetan Plateau. *J. Climate*, **26**, 206–214.
- Betts, A., and C. Jakob, 2002: Study of diurnal cycle of convective precipitation over Amazonia using a single column model. *J. Geophys. Res.*, **107**, 4732, doi:10.1029/2002JD002264.
- Biasutti, M., and A. Giannini, 2006: Robust Sahel drying in response to late 20th century forcings. *Geophys. Res. Lett.*, **33**, L11706, doi:10.1029/2006GL026067.

- , I. M. Held, A. H. Sobel, and A. Giannini, 2008: SST forcings and Sahel rainfall variability in simulations of the twentieth and twenty-first centuries. *J. Climate*, **21**, 3471–3486.
- Bony, S., M. Webb, C. Bretherton, S. Klein, P. Siebesma, G. Tselioudis, and M. Zhang, 2011: CFMIP: Towards a better evaluation and understanding of clouds and cloud feedbacks in CMIP5 models. *CLIVAR Exchanges*, No. 56, International CLIVAR Project Office, Southampton, United Kingdom, 20–24.
- Boone, A. A., I. Poccarr-Leclercq, Y. Xue, J. Feng, and P. de Rosnay, 2010: Evaluation of the WAMME model surface fluxes using results from the AMMA land-surface model intercomparison project. *Climate Dyn.*, **35**, 127–142, doi:10.1007/s00382-009-0653-1.
- Bouniol, D., J. Delanoë, C. Duroure, A. Protat, V. Giraud, and G. Penide, 2010: Microphysical characterisation of West African MCS anvils. *Quart. J. Roy. Meteor. Soc.*, **136** (S1), 323–344, doi:10.1002/qj.557.
- , F. Couvreur, P.-H. Kamsu-Tamo, M. Leplay, F. Guichard, F. Favot, and E. O'Connor, 2012: Diurnal and seasonal cycles of cloud occurrences, types, and radiative impact over West Africa. *J. Appl. Meteor. Climatol.*, **51**, 534–553.
- Chauvin, F., R. Roehrig, and J.-P. Lafore, 2010: Intraseasonal variability of the Saharan heat low and its link with mid-latitudes. *J. Climate*, **23**, 2544–2561.
- Chikira, M., and M. Sugiyama, 2010: A cumulus parameterization with state-dependent entrainment rate. Part I: Description and sensitivity to temperature and humidity profiles. *J. Atmos. Sci.*, **67**, 2171–2193.
- Chou, C., and J. D. Neelin, 2003: Mechanisms limiting the northward extent of the northern summer monsoons over North America, Asia, and Africa. *J. Climate*, **16**, 406–425.
- , —, C.-A. Chen, and J.-Y. Tu, 2009: Evaluating the rich-get-richer mechanism in tropical precipitation change under global warming. *J. Climate*, **22**, 1982–2005.
- Collins, W. J., and Coauthors, 2008: Evaluation of the HadGEM2 model. Met Office Tech. Note 74, 47 pp.
- Cook, K. H., 2008: Climate science: The mysteries of Sahel droughts. *Nat. Geosci.*, **1**, 647–648.
- , and E. K. Vizy, 2006: Coupled model simulations of the West African monsoon system: Twentieth- and twenty-first-century simulations. *J. Climate*, **19**, 3681–3703.
- Del Genio, A. D., 2012: Representing the sensitivity of convective cloud systems to tropospheric humidity in general circulation models. *Surv. Geophys.*, **33**, 637–656, doi:10.1007/s10712-011-9148-9.
- Depraetere, C., M. Gosse, S. Ploix, and H. Laurent, 2009: The organization and kinematics of tropical rainfall systems ground tracked at mesoscale with gages: First results from the campaign 1999–2006 on the Upper Ouémé Valley (Benin). *J. Hydrol.*, **375**, 143–160.
- Dhonneur, G., 1981: Les amas nuageux mobiles: Principale composante de la météorologie du Sahel. *Météorologie*, **27**, 75–82.
- Ding, H., N. S. Keenlyside, and M. Latif, 2012: Impact of the equatorial Atlantic on the El Niño Southern Oscillation. *Climate Dyn.*, **38**, 1965–1972, doi:10.1007/s00382-011-1097-y.
- Donner, L. J., and Coauthors, 2011: The dynamical core, physical parameterizations, and basic simulation characteristics of the atmospheric component of the GFDL global coupled model CM3. *J. Climate*, **24**, 3484–3519.
- Dufresne, J.-L., and Coauthors, 2013: Climate change projections using the IPSL-CM5 Earth system model: From CMIP3 to CMIP5. *Climate Dyn.*, **40**, 2123–2165, doi:10.1007/s00382-012-1636-1.
- Emori, S., T. Nozawa, A. Numaguti, and I. Uno, 2001: Importance of cumulus parameterization for precipitation simulation over East Asia in June. *J. Meteor. Soc. Japan*, **79**, 939–947.
- Fink, A. H., and A. Reiner, 2003: Spatiotemporal variability of the relation between African easterly waves and West African squall lines in 1998 and 1999. *J. Geophys. Res.*, **108**, 4332, doi:10.1029/2002JD002816.
- , D. G. Vincent, and V. Emert, 2002: Rainfall types in the West African Sudanian zone during the summer monsoon 2002. *Mon. Wea. Rev.*, **134**, 2143–2164.
- Gent, P. R., and Coauthors, 2011: The Community Climate System Model version 4. *J. Climate*, **24**, 4973–4991.
- Giannini, A., R. Saravanan, and P. Chang, 2003: Oceanic forcing of Sahel rainfall on interannual to interdecadal timescales. *Science*, **302**, 1027–1030.
- Grandpeix, J.-Y., and J.-P. Lafore, 2010: A density current parameterization coupled with Emanuel's convection scheme. Part I: The models. *J. Atmos. Sci.*, **67**, 881–897.
- Guichard, F., and Coauthors, 2004: Modeling the diurnal cycle of deep precipitating convection over land with cloud-resolving models and single-column models. *Quart. J. Roy. Meteor. Soc.*, **130**, 3139–3172.
- , L. Kergoat, E. Mougin, F. Timouk, F. Baup, P. Hiernaux, and F. Lavenu, 2009: Surface thermodynamics and radiative budget in the Sahelian Gourma: Seasonal and diurnal cycles. *J. Hydrol.*, **375**, 161–177.
- Hazeleger, W., and Coauthors, 2010: EC-Earth: A seamless Earth system prediction approach in action. *Bull. Amer. Meteor. Soc.*, **91**, 1357–1363.
- Held, I. M., T. L. Delworth, J. Lu, K. L. Findell, and T. R. Knutson, 2005: Simulation of Sahel drought in the 20th and 21st centuries. *Proc. Natl. Acad. Sci. USA*, **102**, 17 891–17 896.
- Hoerling, M., J. Hurrell, J. Eischeid, and A. Phillips, 2006: Detection and attribution of twentieth-century northern and southern African rainfall change. *J. Climate*, **19**, 3989–4008.
- Hourdin, F., and Coauthors, 2010: AMMA-Model Intercomparison Project. *Bull. Amer. Meteor. Soc.*, **91**, 95–104.
- , and Coauthors, 2013: LMDZ5B: The atmospheric component of the IPSL climate model with revisited parameterizations for clouds and convection. *Climate Dyn.*, **40**, 2193–2222, doi:10.1007/s00382-012-1343-y.
- Huang, B., Z.-Z. Hu, and B. Jha, 2007: Evolution of model systematic errors in the tropical Atlantic Basin from coupled climate hindcasts. *Climate Dyn.*, **28**, 661–682, doi:10.1007/s00382-006-0223-8.
- Huffman, G. J., R. F. Adler, M. M. Morrissey, D. T. Bolvin, S. Curtis, R. Joyce, B. McGavock, and J. Susskind, 2001: Global precipitation of one-degree daily resolution from multisatellite observations. *J. Hydrometeorol.*, **2**, 36–50.
- , and Coauthors, 2007: The TRMM Multisatellite Precipitation Analysis (TMPA): Quasi-global, multiyear, combined-sensor precipitation estimates at fine scales. *J. Hydrometeorol.*, **8**, 38–55.
- Janicot, S., F. Mounier, N. Hall, S. Leroux, B. Sultan, and G. Kiladis, 2009: The West African monsoon dynamics. Part IV: Analysis of 25–90-day variability of convection and the role of the Indian monsoon. *J. Climate*, **22**, 1541–1565.
- , —, S. Gervois, B. Sultan, and G. Kiladis, 2010: The dynamics of the West African monsoon. Part V: The detection

- and role of the dominant modes of convectively coupled equatorial Rossby waves. *J. Climate*, **23**, 4005–4024.
- , and Coauthors, 2011: Intraseasonal variability of the West African monsoon. *Atmos. Sci. Lett.*, **12**, 58–66, doi:10.1002/asl.280.
- Joly, M., and A. Voltaire, 2009: Influence of ENSO on the West African monsoon: Temporal aspects and atmospheric processes. *J. Climate*, **22**, 3193–3210.
- Jones, C. G., F. Giorgi, and G. Asrar, 2011: The Coordinated Regional Downscaling Experiment: CORDEX—An international downscaling link to CMIP5. *CLIVAR Exchanges*, No. 56, International CLIVAR Project Office, Southampton, United Kingdom, 34–39.
- Kiladis, G. N., C. D. Thorncroft, and N. M. J. Hall, 2006: Three-dimensional structure and dynamics of African easterly waves. Part I: Observations. *J. Atmos. Sci.*, **63**, 2212–2230.
- Kirkevåg, A., T. Iversen, O. Seland, J. B. Debernard, T. Storelvmo, and J. E. Kristjánsson, 2008: Aerosol–cloud–climate interactions in the climate model CAM-Oslo. *Tellus*, **60A**, 492–512.
- Knippertz, P., and M. C. Todd, 2012: Mineral dust aerosols over the Sahara: Meteorological controls on emission and transport and implications for modeling. *Rev. Geophys.*, **50**, RG1007, doi:10.1029/2011RG000362.
- Kothe, S., and B. Ahrens, 2010: On the radiation budget in regional climate simulations of West Africa. *J. Geophys. Res.*, **115**, D23120, doi:10.1029/2010JD014331.
- Lau, K. M., S. S. P. Shen, K.-M. Kim, and H. Wang, 2006: A multimodel study of the twentieth-century simulations of Sahel drought from the 1970s to 1990s. *J. Geophys. Res.*, **111**, D07111, doi:10.1029/2005JD006281.
- Lavaysse, C., C. Flamant, S. Janicot, D. J. Parker, J.-P. Lafore, B. Sultan, and J. Pelon, 2009: Seasonal evolution of the West African heat low: A climatological perspective. *Climate Dyn.*, **33**, 313–330, doi:10.1007/s00382-009-0553-4.
- Lebel, T., and A. Ali, 2009: Recent trends in the central and western Sahel rainfall regime (1990–2007). *J. Hydrol.*, **375**, 52–64.
- , and Coauthors, 2009: AMMA-CATCH studies in the Sahelian region of West Africa: An overview. *J. Hydrol.*, **375**, 3–13.
- , and Coauthors, 2010: The AMMA field campaigns: Multi-scale and multidisciplinary observations in the West African region. *Quart. J. Roy. Meteor. Soc.*, **136** (S1), 8–33.
- Le Lay, M., and S. Galle, 2005: Seasonal cycle and interannual variability of rainfall at hydrological scales: The West African monsoon in a Sudanese climate. *Hydrol. Sci. J.*, **50**, 509–524.
- Liebmann, B., and C. A. Smith, 1996: Description of a complete (interpolated) outgoing longwave radiation dataset. *Bull. Amer. Meteor. Soc.*, **77**, 1275–1277.
- Lin, J.-L., and Coauthors, 2006: Tropical intraseasonal variability in 14 IPCC AR4 climate models. Part I: Convective signals. *J. Climate*, **19**, 2665–2690.
- Loeb, N. G., B. A. Wielicki, D. R. Doelling, G. L. Smith, D. F. Keyes, S. Kato, N. Manalo-Smith, and T. Wong, 2009: Towards optimal closure of the earth's top-of-atmosphere radiation budget. *J. Climate*, **22**, 748–766.
- Mathon, V., H. Laurent, and T. Lebel, 2002: Mesoscale convective system rainfall in the Sahel. *J. Appl. Meteor.*, **41**, 1081–1092.
- Matthews, A. J., 2004: Intraseasonal variability over tropical Africa during northern summer. *J. Climate*, **17**, 2427–2440.
- Meehl, G. A., and Coauthors, 2007a: Global climate projection. *Climate Change 2007: The Physical Science Basis*, S. Solomon et al., Eds., Cambridge University Press, 747–845.
- , C. Covey, T. Delworth, M. Latif, B. McAvaney, J. F. B. Mitchell, R. J. Stouffer, and K. E. Taylor, 2007b: The WCRP CMIP3 multimodel dataset: A new era in climate change research. *Bull. Amer. Meteor. Soc.*, **88**, 1383–1394.
- Miller, M. A., and A. Slingo, 2007: The ARM Mobile Facility and its first international deployment: Measuring flux divergence in West Africa. *Bull. Amer. Meteor. Soc.*, **88**, 1229–1244.
- Mitchell, T. D., and P. D. Jones, 2005: An improved method of constructing a database of monthly climate observations and associated high-resolution grids. *Int. J. Climatol.*, **25**, 673–712, doi:10.1002/joc.1181.
- Mizuta, R., and Coauthors, 2012: Climate simulations using MRI-AGCM3.2 with 20-km grid. *J. Meteor. Soc. Japan*, **90A**, 233–258.
- Mounier, F., and S. Janicot, 2004: Evidence of two independent modes of convection at intraseasonal timescale in the West African summer monsoon. *Geophys. Res. Lett.*, **31**, L16116, doi:10.1029/2004GL020665.
- , —, and G. N. Kiladis, 2008: The West African monsoon dynamics. Part III: The quasi-biweekly zonal dipole. *J. Climate*, **21**, 1911–1928.
- Neale, R. B., and Coauthors, 2010a: Description of the NCAR Community Atmospheric Model (CAM4.0). NCAR Tech. Note NCAR/TN-485+STR, 212 pp. [Available online at http://www.cesm.ucar.edu/models/ccsm4.0/cam/docs/description/cam4_desc.pdf.]
- , and Coauthors, 2010b: Description of the NCAR Community Atmospheric Model (CAM5.0). NCAR Tech. Note NCAR/TN-486+STR, 268 pp. [Available online at www.cesm.ucar.edu/models/ccsm5.0/cam/docs/description/cam5_desc.pdf.]
- Nicholson, S. E., 1980: The nature of rainfall fluctuations in subtropical West Africa. *Mon. Wea. Rev.*, **108**, 473–487.
- , B. Some, and B. Kone, 2000: An analysis of recent rainfall conditions in West Africa, including the rainy seasons of the 1997 El Niño and the 1998 La Niña years. *J. Climate*, **13**, 2628–2640.
- Nikulin, G., and Coauthors, 2012: Precipitation climatology in an ensemble of CORDEX-Africa regional climate simulations. *J. Climate*, **25**, 6057–6078.
- Paeth, H., and A. Hense, 2004: SST versus climate change signals in West African rainfall: 20th-century variations and future projections. *Climatic Change*, **65**, 179–208.
- Pan, D.-M., and D. A. Randall, 1998: A cumulus parameterization with prognostic closure. *Quart. J. Roy. Meteor. Soc.*, **124**, 949–981.
- Pohl, B., and H. Douville, 2011: Diagnosing GCM errors over West Africa using relaxation experiments. Part I: Summer monsoon climatology and interannual variability. *Climate Dyn.*, **37**, 1293–1312, doi:10.1007/s00382-010-0911-2.
- Ramel, R., H. Gallée, and C. Messenger, 2006: On the northward shift of the West African monsoon. *Climate Dyn.*, **26**, 429–440, doi:10.1007/s00382-005-0093-5.
- Redelsperger, J.-L., C. D. Thorncroft, A. Diedhiou, T. Lebel, D. J. Parker, and J. Polcher, 2006: African Monsoon Multidisciplinary Analysis: An international research project and field campaign. *Bull. Amer. Meteor. Soc.*, **87**, 1739–1746.
- Richter, I., and S.-P. Xie, 2008: On the origin of equatorial Atlantic biases in coupled general circulation models. *Climate Dyn.*, **31**, 587–598, doi:10.1007/s00382-008-0364-z.

- Rickenbach, T., R. N. Ferreira, N. Guy, and E. Williams, 2009: Radar-observed squall line propagation and the diurnal cycle of convection in Niamey, Niger, during the 2006 African Monsoon and Multidisciplinary Analyses intensive observing period. *J. Geophys. Res.*, **114**, D03107, doi:10.1029/2008JD010871.
- Rienecker, M. M., and Coauthors, 2011: MERRA: NASA's Modern-Era Retrospective Analysis for Research and Applications. *J. Climate*, **24**, 3624–3648.
- Rio, C., and F. Hourdin, 2008: A thermal plume model for convective boundary layer: Representation of cumulus clouds. *J. Atmos. Sci.*, **65**, 407–425.
- , and Coauthors, 2013: Control of deep convection by subcloud lifting processes: The ALP closure in the LMDZ5B general circulation model. *Climate Dyn.*, **40**, 2271–2292, doi:10.1007/s00382-012-1506-x.
- Roehrig, R., 2010: Variabilité intrasaisonnière de la mousson africaine: Caractérisation et modélisation (Intraseasonal variability of the West African monsoon: Characterization and modeling). Ph.D. dissertation Paris-Est University, 395 pp.
- , F. Chauvin, and J.-P. Lafore, 2011: 10-25-day intraseasonal variability of convection over the Sahel: A role of the Saharan heat low and midlatitudes. *J. Climate*, **24**, 5863–5878.
- Rotstayn, L., M. Collier, M. Dix, Y. Feng, H. Gordon, S. O'Farrell, I. Smith, and J. Syktus, 2010: Improved simulation of Australian climate and ENSO-related climate variability in a GCM with interactive aerosol treatment. *Int. J. Climatol.*, **30**, 1067–1088, doi:10.1002/joc.1952.
- Ruti, P. M., and A. Dell'Aquila, 2010: The twentieth century African easterly waves in reanalysis systems and IPCC simulations, from intra-seasonal to inter-annual variability. *Climate Dyn.*, **35**, 1099–1117, doi:10.1007/s00382-010-0894-z.
- Saha, S., and Coauthors, 2010: The NCEP Climate Forecast System Reanalysis. *Bull. Amer. Meteor. Soc.*, **91**, 1015–1057.
- Sane, Y., and Coauthors, 2012: An analysis of the diurnal cycle of precipitation over Dakar using local rain-gauge data and a general circulation model. *Quart. J. Roy. Meteor. Soc.*, **138**, 2182–2195, doi:10.1002/qj.1932.
- Simmons, A., S. Uppala, D. Dee, and S. Kobayashi, 2007: ERA-Interim: New ECMWF reanalysis products from 1989 onwards. *ECMWF Newsletter*, No. 110, ECMWF, Reading, United Kingdom, 25–35.
- Slingo, A., H. E. White, N. A. Bharmal, and G. J. Robinson, 2009: Overview of observations from the RADAGAST experiment in Niamey, Niger: 2. Radiative fluxes and divergences. *J. Geophys. Res.*, **114**, D00E04, doi:10.1029/2008JD010497.
- Slingo, J., 1980: A cloud parameterization scheme derived from GATE data for use with a numerical model. *Quart. J. Roy. Meteor. Soc.*, **106**, 747–770.
- Stackhouse, P. W., Jr., S. K. Gupta, S. J. Cox, J. C. Mikovitz, T. Zhang, and L. M. Hinkelman, 2011: The NASA/GEWEX Surface Radiation Budget Release 3.0: 24.5-year dataset. *GEWEX News*, No. 21, International GEWEX Project Office, Silver Spring, MD, 10–12.
- Stephens, G. L., and Coauthors, 2010: Dreary state of precipitation in global models. *J. Geophys. Res.*, **115**, D24211, doi:10.1029/2010JD014532.
- Sultan, B., and S. Janicot, 2000: Abrupt shift of the ITCZ over West Africa and intra-seasonal variability. *Geophys. Res. Lett.*, **27**, 3353–3356.
- , and —, 2003: The West African monsoon dynamics. Part II: The “preonset” and “onset” of the summer monsoon. *J. Climate*, **16**, 3407–3427.
- , C. Baron, M. Dingkuhn, and S. Janicot, 2005: Agricultural impacts of large-scale variability of the West African monsoon. *Agric. For. Meteorol.*, **128**, 93–110.
- Taylor, K. E., R. J. Stouffer, and G. A. Meehl, 2012: An overview of CMIP5 and the experiment design. *Bull. Amer. Meteor. Soc.*, **93**, 485–498.
- Thorncroft, C. D., and D. P. Rowell, 1998: Interannual variability of African wave activity in a general circulation model. *Int. J. Climatol.*, **18**, 1305–1323.
- , and M. Blackburn, 1999: Maintenance of the African easterly jet. *Quart. J. Roy. Meteor. Soc.*, **125**, 763–786.
- Timouk, F., and Coauthors, 2009: Response of surface energy balance to water regime and vegetation development in a central Sahelian landscape. *J. Hydrol.*, **375**, 178–189, doi:10.1016/j.jhydrol.2009.04.022.
- Tippett, M., and A. Giannini, 2006: Potentially predictable components of African summer rainfall in a SST-forced GCM simulation. *J. Climate*, **19**, 3133–3144.
- Vannière, B., E. Guilyardi, G. Madec, F. J. Doblas-Reyes, and S. Woolnough, 2013: Using seasonal hindcasts to understand the origin of the equatorial cold tongue bias in CGCMs and its impact on ENSO. *Climate Dyn.*, **40**, 963–981, doi:10.1007/s00382-012-1429-6.
- Vizy, E. K., K. H. Cook, J. Crétaf, and N. Neupane, 2013: Projections of a wetter Sahel in the twenty-first century from global and regional models. *J. Climate*, **26**, 4664–4687.
- Volodire, A., and Coauthors, 2013: The CNRM-CM5.1 global climate model: Description and basic evaluation. *Climate Dyn.*, **40**, 2091–2121, doi:10.1007/s00382-011-1259-y.
- Volodin, E. M., N. A. Diansky, and A. V. Gusev, 2010: Simulating present-day climate with the INMCM4.0 coupled model of the atmospheric and oceanic general circulations. *Izv. Atmos. Oceanic Phys.*, **46**, 414–431.
- Waliser, D. E., J.-L. Li, T. L'Ecuyer, and W.-T. Chen, 2011: The impact of precipitating ice and snow on the radiation balance in global climate models. *Geophys. Res. Lett.*, **38**, L06802, doi:10.1029/2010GL046478.
- Wang, W., P. Xie, S.-H. Yoo, Y. Xue, A. Kumar, and X. Wu, 2011: An assessment of the surface climate in the NCEP climate forecast system reanalysis. *Climate Dyn.*, **37**, 1601–1620, doi:10.1007/s00382-010-0935-7.
- Ward, M. N., 1998: Diagnosis and short-lead time prediction of summer rainfall in tropical North Africa at interannual and multidecadal timescales. *J. Climate*, **11**, 3167–3191.
- Washington, R., and Coauthors, 2012: Fenec: The Saharan climate system. *Proc. Fourth Int. AMMA Conf.*, Toulouse, France, AMMA, PL1.3. [Available online at amma-conf2012.ipsl.fr/data/documents/PL1_3WashingtonLR.pdf.]
- Watanabe, M., and Coauthors, 2010: Improved climate simulation by MIROC5: Mean states, variability, and climate sensitivity. *J. Climate*, **23**, 6312–6335.
- Wielicki, B. A., B. R. Barkstrom, E. F. Harrison, R. B. Lee III, G. L. Smith, and J. E. Cooper, 1996: Clouds and the Earth's Radiant Energy System (CERES): An Earth observing system experiment. *Bull. Amer. Meteor. Soc.*, **77**, 853–868.
- Williams, K. D., and Coauthors, 2013: The Transpose-AMIP II experiment and its application to the understanding of Southern Ocean cloud biases in climate models. *J. Climate*, **26**, 3258–3274.
- Wu, T., and Coauthors, 2010: The Beijing Climate Center atmospheric general circulation model (BCC-AGCM2.0.1): De-

- scription and its performance for the present-day climate. *Climate Dyn.*, **34**, 123–147.
- Xie, P., and P. A. Arkin, 1997: Global precipitation: A 17-year monthly analysis based on gauge observation, satellite estimates, and numerical model outputs. *Bull. Amer. Meteor. Soc.*, **78**, 2539–2558.
- Xue, Y., and Coauthors, 2010: Intercomparison and analyses of the climatology of the West African Monsoon in the West African Monsoon Modeling and Evaluation project (WAMME) first model intercomparison experiment. *Climate Dyn.*, **35**, 3–28, doi:10.1007/s00382-010-0778-2.
- Yang, S., K.-S. Kuo, and E. A. Smith, 2008: Persistent nature of secondary diurnal modes of precipitation over oceanic and continental regimes. *J. Climate*, **21**, 4115–4131.
- Yokimoto, S., and Coauthors, 2011: Meteorological Research Institute-Earth System Model version 1 (MRI-ESM1)—Model description. MRI Tech. Rep. 64, Meteorological Research Institute, Japan, 83 pp.